



UNIVERSITÀ DI PISA

MASTER THESIS IN PHYSICS

Optimizing the sensitivity to the $\tau \rightarrow \ell\gamma$ decay with a novel tag approach at Belle II

MASTER CANDIDATE

Maria Antonietta Palaia

SUPERVISOR

Prof. Francesco Forti

University of Pisa

CO-SUPERVISOR

Dott. Francesco Tenchini

University of Pisa

ACADEMIC YEAR
2021/2022

*To my family
and friends*

Abstract

The measurement of the $\tau \rightarrow \ell\gamma$ decay, where ℓ can be a muon or an electron, is of great interest for high energy physics. In the Standard Model, where charged lepton flavour is conserved, this decay is heavily suppressed and can only occur at loop level with very low probability ($\sim O(10^{-54})$). However, several new physics models predict scenarios where this decay is more likely to occur, with probabilities up to 10^{-10} . A positive detection of a signal would represent an indisputable evidence of physics beyond the Standard Model, but also improving the experimental limit of this measurement is important to constrain a wide class of possible Standard Model extensions.

The current best measurements for $\text{BR}(\tau \rightarrow \mu\gamma)$ and $\text{BR}(\tau \rightarrow e\gamma)$ have been reported by the Belle and BaBar collaborations, with upper limits of 4.2 and 3.3×10^{-8} , respectively. Both experiments used data coming from electron-positron collisions at the $\Upsilon(4S)$ resonance energy in the centre of mass system.

Belle II, the successor experiment of Belle, collected 424 fb^{-1} of data so far, corresponding to about $4 \cdot 10^8$ τ pairs, and is expected to collect up to 50 ab^{-1} in the coming years, corresponding to more than 10^{10} τ pairs. With this amount of data it will be possible to greatly improve the sensitivity to the $\tau \rightarrow \ell\gamma$ search.

In this thesis, I developed the selection criteria for a measurement of the $\tau \rightarrow \ell\gamma$ decay, using $\tau^+\tau^-$ events. The Belle II analysis searches for an event in which one of the two τ 's (signal) decays as $\tau \rightarrow \ell\gamma$, while the other one (tag) decays generically, according to the known SM processes. The previous measurement of the $\tau \rightarrow \ell\gamma$ at Belle adopted a one-prong tag approach, in which an event is identified through the τ decays in one charged particle. Instead, I will focus on events identified by tag τ decaying in three charged particles (referred to as *three-prong tag* mode), a channel dominated by the $\tau \rightarrow 3\pi(\pi^0)\nu$ process. The three-prong topology is more constrained than the one-prong one, allowing an efficient selection with low background. The three-prong tag can be combined with the existing one-prong selection, increasing the statistical power of the analysis at a given luminosity. This work shows the potential, related to more inclusive approaches, to increase the sensitivity of the data at Belle II.

Contents

1	Theoretical Overview	1
1.1	Phenomenology of the Standard Model	1
1.1.1	Elementary particles	3
1.1.2	Fundamental interactions	4
1.1.3	Particle masses	5
1.2	Open questions of the Standard Model	6
1.3	Neutrino oscillations	9
1.3.1	The PMNS Matrix	10
1.4	Lepton Flavour Violation in the Standard Model	11
1.4.1	Lepton Flavour Violation in τ decays	13
2	The Belle II Detector	15
2.1	Accelerator Design	15
2.2	Vertex Detector	17
2.2.1	Pixel Vertex Detector	17
2.2.2	Silicon Vertex Detector	19
2.3	Central Drift Chamber	22
2.4	Particle Identification system	24
2.4.1	Time of Propagation counter	24
2.4.2	Aerogel Ring-Imaging Cherenkov detector	26
2.5	Electromagnetic Calorimeter	27
2.6	KLM	29
2.6.1	Muon and K_L identification	31
2.7	Trigger system	32
2.7.1	High Level Trigger	32
2.8	Belle II software and computing	33

CONTENTS

3	State of the art of the $\tau \rightarrow \ell\gamma$ search	35
3.1	Lepton flavor violating τ decays	35
3.2	Brief history of the LFV searches	36
3.3	Analysis technique at the B-factories	37
3.3.1	BaBar analysis	41
3.3.2	Belle analysis	44
4	Analysis Overview	49
4.1	Dataset	50
4.1.1	Background Processes	50
4.1.2	Signal Events	51
4.2	Event Reconstruction and Pre-Selections	51
4.2.1	Reconstruction Criteria	51
4.2.2	Pre-Selections	53
4.3	Event Selection and Background Suppression	54
4.3.1	Figure Of Merit	55
4.3.2	Selection variables	56
4.3.3	Simulated Annealing	56
4.4	Optimization of the Selection	58
4.4.1	Optimization Region	58
4.4.2	Signal Region	62
5	Results and Conclusions	67
5.1	Sensitivity Estimate	67
5.1.1	Results of the 3x1 and 1x1 topologies	68
5.1.2	Upper Limit to $\mathcal{B}(\tau \rightarrow \mu\gamma)$	69
5.2	Systematic Uncertainties	70
5.3	Conclusions	71
	References	73
	Acknowledgments	79



Theoretical Overview

The Standard Model (SM) of particle physics is the theory classifying all known elementary particles and describing three of the four known fundamental forces (electromagnetic, weak and strong interactions, omitting gravity).

Although the Standard Model has demonstrated huge successes in providing experimental predictions, it leaves some phenomena unexplained. For example, it does not fully explain the baryon-anti-baryon asymmetry, incorporate the theory of gravitation as described by general relativity and it also does not explain the presence of dark matter and dark energy in the universe.

Searching for Physics Beyond the Standard Model is the chief goal of today's particle physics and it's one of the most active areas of research in both theoretical and experimental physics.

1.1 PHENOMENOLOGY OF THE STANDARD MODEL

The modern idea that the ultimate nature of our universe is discrete originated in ancient Greek atomism. During the 5th century B.C., Greek philosophers Leucippus and Democritus considered the idea that if keeping on cutting matter into smaller and smaller pieces, one eventually end up with an irreducible piece which cannot be further divided. They called this fundamental bit an *atom*. This speculative effort represents, as far as we can trace, the first attempt of mankind to understand the world at a fundamental level.

It goes without saying that many and many centuries of research has considerably refined the concept of atom and we actually have a deeper understanding

1.1. PHENOMENOLOGY OF THE STANDARD MODEL

of what the world is made of. For example, we know that there is no single fundamental particle, but rather a number of them. The properties of these particles and the way they interact with each other are described by a theory known as *Standard Model* (SM).

Our current understanding of elementary particles allows us to know that the ordinary matter that we experience in everyday life consists of only three types of particles: *up* and *down quarks*, which make up protons and neutrons in the nucleus, and *electrons* that surround the nucleus.

The Standard Model includes many other elementary particles, that are summarized in Figure 1.1.

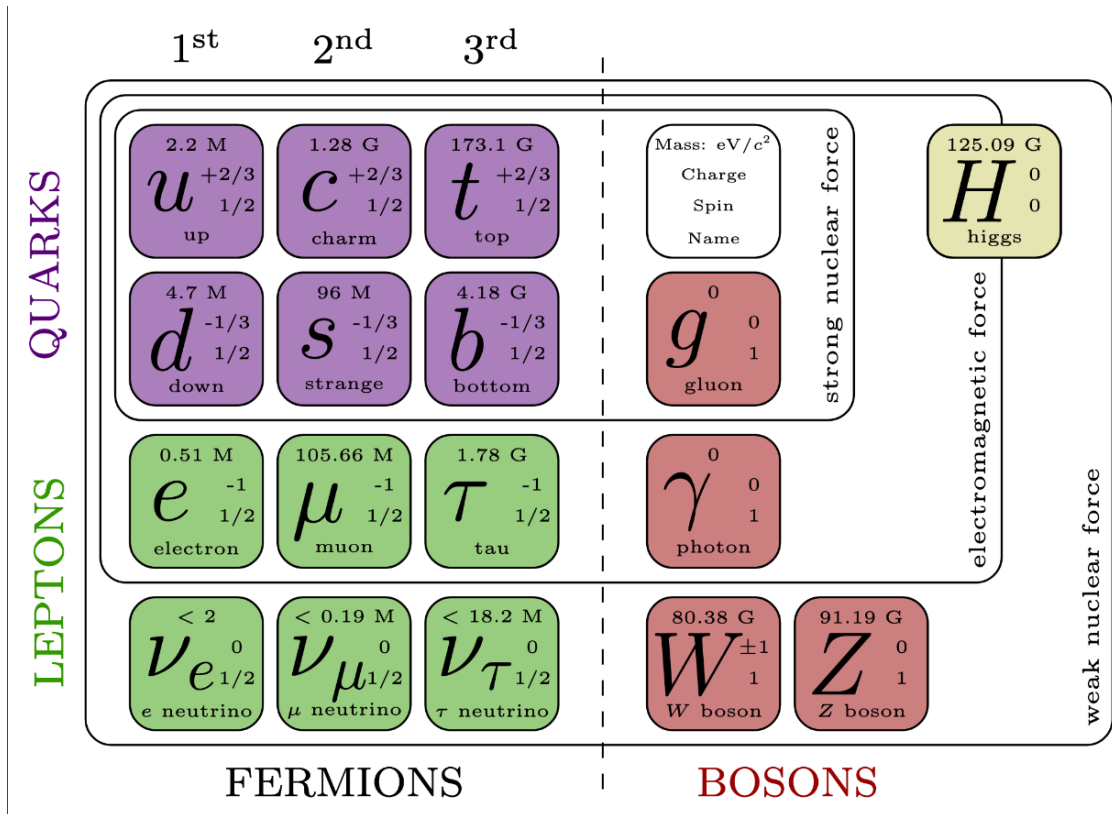


Figure 1.1: A summarized picture of elementary particles and their main properties [1]. Quarks (violet boxes) and leptons (green boxes) are grouped into the three different generations of matter. Red boxes represent the spin-1 bosons, mediators of the fundamental forces. Grey box is the spin-0 Higgs Boson.

1.1.1 ELEMENTARY PARTICLES

Today we know that all matter can be described in terms of two basic kinds of particles: *fermions* and *bosons*, distinguished by their collective properties under the interchange of two particles.

Fermions are half-odd-integer spin particles, following to the Fermi-Dirac statistics, and include all *quarks* and *leptons*. Both quarks and leptons consists of six particles, which are related in three different doublets, or generations. The lightest and most stable particles make up the first generation, whereas the heavier and less-stable particles belong to the second and third generations. Heavier particles quickly decay to lighter and more stable ones. Up and down quarks and electrons belong to the first generation and this represents the reason why all ordinary matter is stable in the universe.

The six leptons are paired in three doublets: the *electron* and the *electron neutrino*, the *muon* and the *muon neutrino*, the *tau* and the *tau neutrino*. The electron, the muon and the tau all have an electric charge and a sizeable mass, whereas the neutrinos are electrically neutral and are expected by the SM to be massless. Each doublet is identified by a different quantum number, the lepton family number, or lepton flavor number, $L_{e,\mu,\tau}$. This quantity is a conserved quantum number in all interactions.

The six quarks are similarly arranged in three generations: the *up* and *down* quarks form the first one, followed by the *charm* and *strange* quarks, then the *top* and the *bottom*. Quarks combine each other in composite particles called hadrons, that contain either a quark and an antiquark pair (mesons) or three quarks (baryons).

As first predicted by Dirac in 1928, all the elementary particles have their corresponding antimatter particles. All the quantum numbers of an antiparticle are the opposite of that of the corresponding particle, except for its mass, which remains unchanged.

The universe as we know exists because the elementary particles interact and influence each other. The interaction between particles is carried out by the exchange of a virtual particle, the force mediators. Bosons, integer value spin particles obeying to the Bose-Einstein statistics, are the force carriers that mediate the fundamental interactions. There are four of these basic forces at work in the universe and all the known interactions in the world are governed by some their combination: the strong force, the weak force, the electromagnetic

1.1. PHENOMENOLOGY OF THE STANDARD MODEL

force, and the gravitational force. Each fundamental force has its own corresponding mediator boson and different properties and manifestations. *Photons* are responsible for the electromagnetic force, that involves the interaction of electric and magnetic fields. This boson is a neutral and massless particle, and as a result, the electromagnetic interaction has infinite range. Similarly, *gluons*, neutral and massless particles too, carry the strong force that keeps the bound states in nuclei. The W and Z bosons mediate the weak force, responsible for nuclear radioactive decays. These particles are very massive, explaining the short interaction range for the weak force. Finally, another boson is supposed to exist in nature, the *graviton*, a spin-2 massless particle, that should be the force carrier of the gravitational force. However, up to now, there is no experimental evidence for its existence.

1.1.2 FUNDAMENTAL INTERACTIONS

Quantum field theory is the mathematical framework for the Standard Model. Each particle is associated with a dynamic field pervading the space-time. Interactions between particles are dictated by symmetry principles, the so-called local gauge symmetries. The SM is a quantum gauge theory based on the symmetry group $U_Y(1) \otimes SU_L(2) \otimes SU_C(3)$. This symmetry group describes the formal operations that can be applied to the fields without changing the dynamics of the system.

In the Glashow-Salam-Weinberg (GSW) model, $SU_L(2) \otimes U_Y(1)$ is the gauge group representing the electroweak interaction, the unified theory describing electromagnetism and weak interaction. The local gauge invariance requires the introduction of the gauge field B_μ , to satisfy the $U(1)$ symmetry, and of the three gauge fields W_μ^a (where $a=1,2,3$), for the $SU(2)$ symmetry. These fields, however, cannot be interpreted as the physical fields of the mediator bosons: since any mass term appearing in the Lagrangian would spoil the gauge invariance property, these fields are all initially massless. The massive vector bosons, Z^0 and W^\pm , are predicted by the spontaneous symmetry breaking of the electroweak symmetry $SU_L(2) \otimes U(1)_Y \rightarrow U(1)$, that triggers the Higgs mechanism: this causes the bosons it interacts with to have mass. The photon A_μ and the weak bosons, Z_μ^0 and W_μ^\pm , become the physical fields of the theory with their explicit mass terms.

$SU_C(3)$ is the symmetry group describing the strong interaction between

quarks. The symmetry group introduces the eight vectorial gauge fields of the gluons, G_{μ}^A , where $A=1, \dots, 8$. Similarly to the electric charge for electromagnetism, the group symmetry brings a conserved quantity for the strong interaction, the colour charge. Quarks, in fact, come in three different colours (red, blue, green) and experiments show that they only mix in such ways as to form colourless objects. This phenomenon is known as "color confinement" and it results being a specific property of the strong interactions only. The presence of a colour charge made the quantum field theory of the strong interaction to be usually referred to as Quantum Chromodynamics (QCD).

The gravitational force is the most obvious force at play around us, but yet it's the one we understand least. In fact, we have a theory of gravity, the Einstein's general theory of relativity that describes gravity and the geometry of the universe on enormous scales. However, gravity turns out to be the weakest of the four fundamental interactions and, as a result, it has no significant influence at sub-atomic scale. This is the main reason why it is not included in the SM. Moreover, it doesn't exist a quantum field theory of the gravity that fits with the description given by Einstein. Most of the current efforts in theoretical physics are to find a way to quantize the gravitational field, resulting in a theory of quantum gravity which could incorporate the gravitational force in a common theoretical framework with the other three forces.

1.1.3 PARTICLE MASSES

The local gauge principle provides an elegant description of the observed interactions in nature and it places also on a solid experimental basis, due to the great successes of the Standard Model in describing and predicting experimental data. However, the required local gauge invariance turns out to be broken by mass terms in the Lagrangian. This means that the local gauge symmetries can be satisfied only if the gauge bosons of the interactions are massless. If this is not a problem for QED and QCD, where the force carriers are indeed massless, it represents a difficult obstacle for the weak interaction, because of the large masses of the W and Z bosons. The Higgs mechanism provides an elegant description of the way the gauge bosons acquire their masses, due to the interactions with the Higgs field. The same mechanism generates also the masses of the other elementary particles. The assumption is made that the universe is filled with a spin-0 field, named the Higgs field, which is a doublet

1.2. OPEN QUESTIONS OF THE STANDARD MODEL

in $SU(2)$ and with a non-zero $U(1)$ hypercharge, but a singlet in a color space. Elementary particles can interact with this field, acquiring mass.

1.2 OPEN QUESTIONS OF THE STANDARD MODEL

Up to date, the Standard Model can be regarded as the most successful theory on particle physics, because it can explain lots of experimental evidence within its framework. The most famous example is the discovery of the Higgs boson, after more than fifty years from its prediction, by the CMS and ATLAS collaborations at the Large Hadron Collider at CERN in 2012 [2]. Other successes include the prediction of the W and Z bosons, the gluon and the top and charm quarks, and the corresponding discoveries. Moreover, the anomalous gyromagnetic moment of the electron gives the best agreement between theory and experiment.

Despite the great successes of the Standard Model, it is well known that there are still several phenomena for which this theory is completely lacking or unsatisfactory. Some of these are actually open questions for all the scientific community and will be briefly discussed as follows.

GRAVITY

As above mentioned, The Standard Model does not include a description of gravity that could be consistent with Einstein's general theory of relativity. The current challenge for theoretical physicists is to elaborate a theory of gravity in which neither gravitational nor quantum effects can be ignored, such as in the vicinity of a black hole, where quantum fluctuations of the space-time play an important role. A theory of quantum gravity is, thus, necessary to describe these quantum effects and this field of research is in active developing.

DARK MATTER

Cosmological observations tell us that the ordinary matter described by the SM accounts for only about 5% of the total mass-energy content of the universe. Over the years, researchers have been able to infer that about 26% of our universe should be made up of *dark matter*, a hypothetical form of matter that must barely interact with ordinary matter and radiation, except through gravity. Dark matter does not absorb, reflect or emit light (hence the name "dark"). These features make it extremely hard to detect directly: physicists have been able to prove its

existence only from its gravitational effects on visible matter which cannot be fully explained by current theories of gravity without the presence of additional and unseen matter in the universe.

One of the first observational evidence for dark matter is related to Vera Rubin and Kent Ford's work, which provided a strong evidence for dark matter studying the rotation curves of the Andromeda galaxy [3]. The curve of rotation describes the number of revolutions of a galaxy according to the distance to the center: the speed of a star in the galaxy is supposed to decrease, following a Keplerian motion, as the distance of the star to the center of the galaxy increases. However it appeared that the speed of the stars located at the periphery of the Andromeda Galaxy remained almost constant when the distance to the center increased: speed did not decrease whereas moving away from the center. In the following years, many other observations were carried out, with similar results. Figure 1.2 shows the fit to the observed data for the rotation curve of the spiral galaxy NGC 3198 [4]. The shape of the rotation curves can be explained by a combination of matter distribution in the galactic disk and an additional component of dark matter surrounding the galaxy.

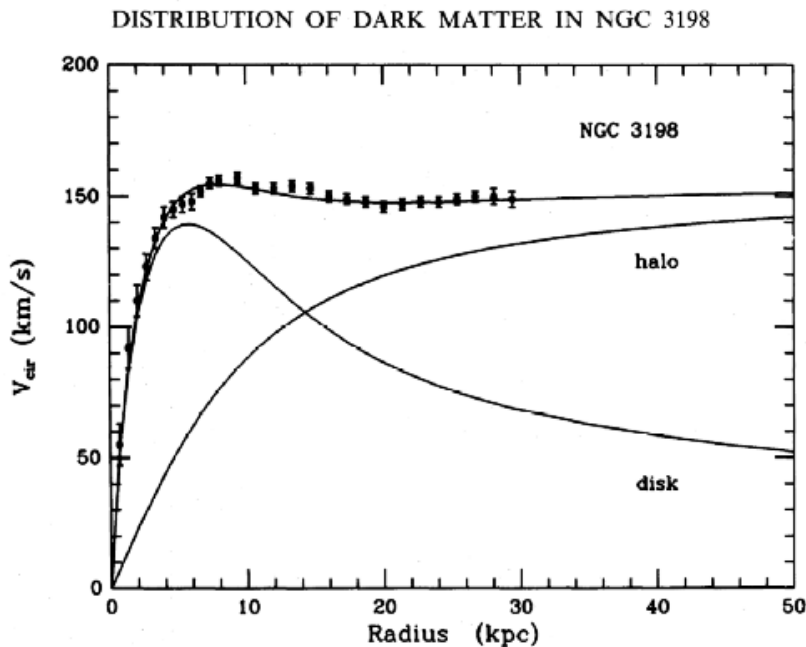


Figure 1.2: The expected rotation curve for the spiral galaxy NGC 3198 assuming an exponential mass disk and a halo of dark matter. Dots with error bars represent the observed data. Image taken from [4].

The Standard Model does not supply any explanation for dark matter. Candi-

1.2. OPEN QUESTIONS OF THE STANDARD MODEL

dates for dark matter are supposed to be some new kind of elementary particles, potentially massive and weakly interacting, that has not yet been discovered. Many experiments aim to search for them.

DARK ENERGY

The remaining energy of the universe should consist of the so-called *dark energy*, an unknown form of energy that affects the cosmos on large scale. Current observations indicate that the content of dark energy is uniform in our universe and contributes for about 69% of the total energy.

It came the 1998 when observations of very distant supernovae showed that the universe is not expanding at a constant rate, but rather, it's speeding up [5]. This acceleration may be due to "*something very fundamental that nobody could have anticipated just by looking at the Standard Model*".

The time evolution of the cosmic scale factor, in fact, depends on the composition of mass-energy in the universe. While the amount of matter contained in the universe contributes to decelerate its expansion, its dynamics may also be affected by exotic forms of energy. Among these is a possible energy of the vacuum, representing some properties of the space-time itself. Empty space, in fact, can possess its own energy: as more space come into existence, more of this vacuum energy would appear. It's just this form of energy the would cause our universe to expand faster and faster. This explanation represents one of the possible interpretations of what goes under the name of dark energy. Other hypothesis on the origin and the presence of dark energy in the universe are actually under study and make it a very active target of research.

MATTER-ANTIMATTER ASYMMETRY

The Standard Model predicts that at the moment of the Big Bang an equal amount of matter and antimatter should have been created in the early universe. If matter and antimatter particles are created and destroyed in pairs, it seems the universe should contain nothing but leftover energy. However, today we observe an universe made out of mostly matter and also in our daily life, everything we see is made almost entirely of matter. This phenomenon is known as matter-antimatter asymmetry, consisting in the imbalance of baryonic matter over the anti-baryonic matter. Actually there is no reason and no explanation for why this should be so. It is likely that some physical law have acted differently for matter

and antimatter during the process of evolution of the universe and one of the current challenges in particle physics is to figure out why we see an asymmetry between matter and antimatter.

NEUTRINO MASSES

According to the Standard Model, neutrinos come in three different flavours (ν_e, ν_μ, ν_τ) and should be massless and chargeless particles that undergo only weak interactions. However, it has been observed that neutrinos can transform into one another, as they move. This phenomenon came to be known as *neutrino oscillations*. The flavour change observed in neutrinos can be explained only assuming that they do have mass and that neutrino flavours have significant mixing.

Mass terms for the neutrinos can be added to the Standard Model by hand, even if this leads to new theoretical problems, since it is not clear if the way neutrinos acquire mass is the same that other fundamental particles do in the Standard Model.

1.3 NEUTRINO OSCILLATIONS

In the 1960s, the first measurements of the flux of electron neutrinos arriving from the core of the Sun have been made by the astrophysicist Raymond Davis, Jr. [6]. The result of the observation was that the value of solar neutrinos detected was about 1/3 of the number predicted by the calculations of John N. Bahcall [7], making this discrepancy known to the scientific community as *solar neutrino problem*. Many other experiments were performed in the following years with the same purpose, such as GALLEX in Italy, Super Kamiokande in Japan, and SNO (Sudbury Neutrino Observatory) in Ontario. Especially these last two experiments demonstrate undoubtedly that solar and atmospheric neutrinos can change their flavours during their propagation [8] [9]: this explanation finally solved the solar neutrino problem becoming the more strong evidence of neutrino oscillations.

In the past few decades, several experiments have confirmed the event of flavour change with neutrinos produced from other sources, such as atmospheric, reactor and accelerator sources.

1.3. NEUTRINO OSCILLATIONS

1.3.1 THE PMNS MATRIX

The observation of neutrino oscillation shows clearly that neutrinos have masses. As above mentioned, this feature can be included into the Standard Model, even if it is still not clear the mechanism of mass generation.

Similarly to the CKM quark mixing matrix, the neutrinos flavour eigenstates can be written as a combination of mass eigenstates. The relationship between flavor and mass eigenstates is described by the *Pontecorvo-Maki-Nakagawa-Sakata (PMNS) matrix*. The PMNS matrix was introduced in 1962 by Maki, Nakagawa and Sakata [10] to explain the neutrino oscillations predicted for the first time by Bruno Pontecorvo in 1957 [11].

In the Standard Model, $\{\nu_\alpha\}$ where $\alpha = e, \mu, \tau$, are the three eigenstates of the weak interaction that form a complete basis for the neutrinos. Another possible basis is defined by the neutrino states of definite mass, $\{\nu_i\}$ where $i=1,2,3$, that diagonalize the free particle Hamiltonian. The unitary transformation between the two basis is parametrized by the PMNS matrix, whose components $|U_{\alpha i}|^2$ correspond to the flavour- α fraction in ν_i or, equivalently, mass- i fraction in ν_α :

$$\begin{pmatrix} \nu_e \\ \nu_\mu \\ \nu_\tau \end{pmatrix} = \begin{bmatrix} U_{e1} & U_{e2} & U_{e3} \\ U_{\mu 1} & U_{\mu 2} & U_{\mu 3} \\ U_{\tau 1} & U_{\tau 2} & U_{\tau 3} \end{bmatrix} \begin{pmatrix} \nu_1 \\ \nu_2 \\ \nu_3 \end{pmatrix}. \quad (1.1)$$

The evidence of neutrino oscillation established experimentally that a neutrino of a given flavour α is a superposition of neutrinos with different masses.

Given the transformation in eq (1.1), the probability that a neutrino of flavour will be observed of flavour β after having travelled a distance L is

$$P_{\alpha \rightarrow \beta} = \delta_{\alpha\beta} - 4 \sum_{j>k} \text{Re}\{U_{\alpha j}^* U_{\beta j} U_{\alpha k} U_{\beta k}^*\} \sin^2\left(\frac{\Delta m_{jk}^2 L}{4E}\right) + 2 \sum_{j>k} \text{Im}\{U_{\alpha j}^* U_{\beta j} U_{\alpha k} U_{\beta k}^*\} \sin\left(\frac{\Delta m_{jk}^2 L}{4E}\right) \quad (1.2)$$

where

- $\Delta m_{jk}^2 \equiv m_j^2 - m_k^2$ is the mass difference between neutrinos,
- L is the distance travelled by the neutrino, which in modern experiments it is on the order of km,

- E is the neutrino energy, typically on order of MeV or GeV.

It is important to note that (1.2) contains the term Δm_{jk}^2 , but does not contain explicitly the value of each mass term. From the squared-mass splitting we can, at best, find a range of values for the masses of the mass eigenstates.

In the present description, we are assuming for notational simplicity a total of three mass eigenstates for neutrinos. However, we do not know for sure the total number of mass eigenstates. Actually, from studies on solar and atmospheric neutrinos we can only say that they are at least three. In fact,

- solar neutrinos have a squared-mass splitting of $\Delta m_{sol}^2 = 7.5 \times 10^{-5} \text{eV}^2$ [12]. We attribute this splitting to the ν_1 and ν_2 mass eigenstates, thus $\Delta m_{sol}^2 = m_{\nu_2}^2 - m_{\nu_1}^2$.
- Atmospheric neutrinos have a squared-mass splitting of $\Delta m_{atm}^2 = 0.0025 \text{eV}^2$ [13] [14]. We must have at least another mass eigenstate, said ν_3 , to accommodate for this. We attribute the atmospheric splitting to ν_2 and ν_3 , thus, $\Delta m_{atm}^2 = m_{\nu_3}^2 - m_{\nu_2}^2$.

In the above representation we have assumed $m_3^2 \gg m_2^2 > m_1^2$, but the mass ordering could be different (inverted hierarchy). Nothing prohibits that more than three mass eigenstates exist. If this would be the case, it would give rise to one or more flavours of neutrinos that do not form an isospin doublet with a lepton. This implies that they cannot couple to W or Z bosons and cannot participate in weak interactions. Such exotic neutrinos are called *sterile neutrinos*.

As already said, the $|U_{\alpha i}|^2$ matrix term represents the fraction of ν_α in ν_i . Experimentally, it turns out that $|U_{e3}|^2$ is very small [15]. Correspondingly, a mixing angle can be defined, θ_{13} , such as $|U_{e3}|^2 = \sin^2 \theta_{13}$. Experiments show that $\theta_{13} \sim 9^\circ$ [16], indicating very little mixing. A summary of the experimental observations is reported in Table 1.1.

1.4 LEPTON FLAVOUR VIOLATION IN THE STANDARD MODEL

The lepton flavour conservation postulated in the Standard Model with massless neutrinos is an accidental symmetry, since it is not related to any fundamental invariance principle. The experimental observation of neutrino oscillation has demonstrated that neutrinos are massive and that lepton flavour is violated in the neutral sector.

1.4. LEPTON FLAVOUR VIOLATION IN THE STANDARD MODEL

	ν_e	ν_μ	ν_τ
ν_1	$ U_{e1} ^2 \approx \frac{2}{3}$	$ U_{\mu 1} ^2 \approx \frac{1}{6}$	$ U_{\tau 1} ^2 \approx \frac{1}{6}$
ν_2	$ U_{e2} ^2 \approx \frac{1}{3}$	$ U_{\mu 2} ^2 \approx \frac{1}{3}$	$ U_{\tau 2} ^2 \approx \frac{1}{3}$
ν_3	$ U_{e3} ^2 \ll 1$	$ U_{\mu 3} ^2 \approx \frac{1}{2}$	$ U_{\tau 3} ^2 \approx \frac{1}{2}$

Table 1.1: Table indicating mixing probabilities in neutrinos [17].

Charged Lepton Flavour Violating (cLFV) processes are possible but highly suppressed in the Standard Model. Such transitions can occur only at loop level involving neutrinos and W bosons. An example process violating the lepton flavour is the $\mu \rightarrow e\gamma$ decay, which in the SM occurs via the loop diagram reported in Figure 1.3.

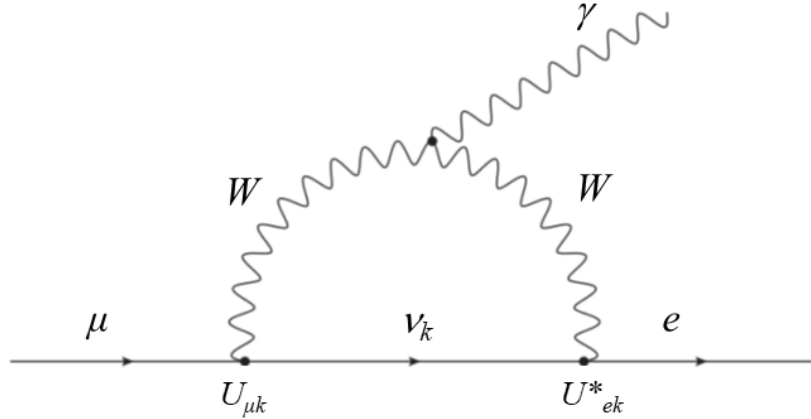


Figure 1.3: Loop diagram contributing to the $\mu \rightarrow e\gamma$ in the Standard Model with massive neutrinos.

This transition is described by an effective μ - e - γ interaction, where the μ - e transition is induced via neutrino oscillations through the PMNS matrix terms $U_{\mu k}, U_{ek}^*$. The decay amplitude is given by

$$\mathcal{M}(\mu \rightarrow e\gamma) = \frac{3\alpha}{32\pi} \left| \sum_{k=1,3} \frac{U_{\mu k} U_{ek}^* m_{\nu k}^2}{M_W^2} \right|^2, \quad (1.3)$$

where a detailed calculation of the decay rate can be found in [18].

Being this process suppressed by the fourth power of the neutrino masses, the resulting numerical value is about $\mathcal{B}(\mu \rightarrow e\gamma) < 10^{-54}$, with the latest measurements of the neutrino masses and mixing. Such branching ratio is too small for the sensitivity of the present-days experiments. An experimental observation of charged LFV would thus be an unambiguous signature of physics beyond the Standard Model. Many experiments, such as MEGA and SINDRUM, have searched for lepton flavour violation in muon decays. The current upper limit to the $\mu \rightarrow e\gamma$ decay has been set by the MEG experiment, with $\mathcal{B}(\mu \rightarrow e\gamma) < 4.2 \times 10^{-13}$ [19].

However, a discovery of $\mu \rightarrow e\gamma$ alone will not provide sufficient information to nail down the underlying lepton flavour violation mechanism. It is critical to probe all lepton flavour violating modes and searches for $\mu \rightarrow e\gamma$ need to be augmented by studies of $\tau \rightarrow \mu\gamma$ as well as $\tau \rightarrow e\gamma$ decays.

1.4.1 LEPTON FLAVOUR VIOLATION IN τ DECAYS

According to our best theory for elementary particles, the Standard Model, the τ lepton is a spin- $\frac{1}{2}$, elementary particle, obeying the Dirac equation [20]. The τ has associated its neutrino, ν_τ , and both the particles have a unique, conserved, lepton number, L_τ . According to this model, all the τ decays require the presence of the tau neutrino in the final state and any decay which does not include the τ neutrino would be an evidence of lepton flavour violation and, thus, of Physics beyond the Standard Model.

τ decays offer a very interesting complementarity to the μ decays in the charged lepton flavour violation. Since the tau lepton is much heavier than the muon, many more types of lepton flavour violating processes can be studied with τ decays. In addition to the $\tau \rightarrow \ell\gamma$ and $\tau \rightarrow \ell\ell^+\ell^-$, where $\ell = e, \mu$, channels (the counterparts of $\mu \rightarrow e\gamma$ and $\mu \rightarrow 3e$), more exotic lepton flavour violating decay processes are accessible to tau leptons. The tau lepton can undergo also semileptonic lepton flavour violating channels, which allow us to test the lepton flavour violating couplings between quarks and leptons. Furthermore, more exotic decay processes, such as $\tau^+ \rightarrow \mu^-e^+e^+$, in which all the lepton flavour symmetries are violated, and $\tau \rightarrow \Lambda\pi$, in which the baryon number is violated, can be searched.

The neutrino-less two body decays, $\tau \rightarrow \mu\gamma$ and $\tau \rightarrow e\gamma$, occur via the same

1.4. LEPTON FLAVOUR VIOLATION IN THE STANDARD MODEL

loop diagram as in Figure 1.3 and the resulting expected branching ratio are of the order of 10^{-53} for both the channels. Again, a similar branching ratio is too far from our experimental sensitivities. However, many different new physics models predict the $\tau \rightarrow \ell\gamma$ decay occurring with much higher probabilities.

In SUperSYmmetric theories (SUSY) [21], and especially in Grand-Unified Theories (SUSY-GUT), tau lepton flavour violation is especially favoured, with branching ratios predicted to lie only 1-2 orders of magnitude lower than the present experimental bounds. Many other New Physics models, such as Super-Symmetric and seesaw [22], supersymmetric standard models [23], little Higgs models [24], extended Higgs models, exhibit strong enhancements of lepton flavour violation in the charged sector with expected branching fractions up to 10^{-10} . Observation of lepton flavour violation in τ decays would be a clear signature of physics beyond the Standard Model, while a non-observation would provide further constraints on the current theoretical models.

Currently, the most stringent limits on the $\tau \rightarrow \ell\gamma$ decay have been obtained by the first generation B-Factory experiments, BaBar and Belle, with limits at the level of 10^{-8} . Further improvements to these measurements are expected from the next generation of the B-Factory experiment, Belle II, which is expected to collect over the next decade 50 ab^{-1} of data. At Belle II a sensitivity at the order of $10^{-9} - 10^{-8}$ is expected allowing physicists to explore a wide region of parameter space in New Physics scenarios.

2

The Belle II Detector

The aim of the new generation (super) B-factory is to improve our knowledge of the flavour sector and to estimate more precisely the Standard Model parameters. The main tool for new discoveries is the Belle II detector. It has been designed to maintain high performances in an environment characterized by high background levels, with an improvement in luminosity and precision with respect to its predecessor, Belle.

The design of Belle II follows to a large extent the scheme of Belle, maintaining a comparable or better performance. An overview of the main components is given in this chapter.

2.1 ACCELERATOR DESIGN

The SuperKEKB facility is designed to collide electrons and positrons with energies in the centre-of-mass in the regions of the $\Upsilon(nS)$ resonance, with most of the data collected at the $\Upsilon(4S)$ resonance. SuperKEKB has a design luminosity of $8 \times 10^{35} \text{cm}^{-2} \text{s}^{-1}$, that is about 80 times larger than that of KEKB. Over the whole period of data taking, it is expected to produce about 10^{10} b , c and τ pairs.

The asymmetric beam energy e^+e^- collider SuperKEKB, see Figure 2.1, has a circumference of about 3 km. The main components are the electron ring, known as the high-energy ring (HER), the positron ring, known as the low-energy ring (LER) and an injection linear accelerator with a 1.1 GeV positron damping ring.

The main modifications in the layout of the Belle II experiment are in the change of an accelerator design. In SuperKEKB, the collider is designed for the

2.1. ACCELERATOR DESIGN

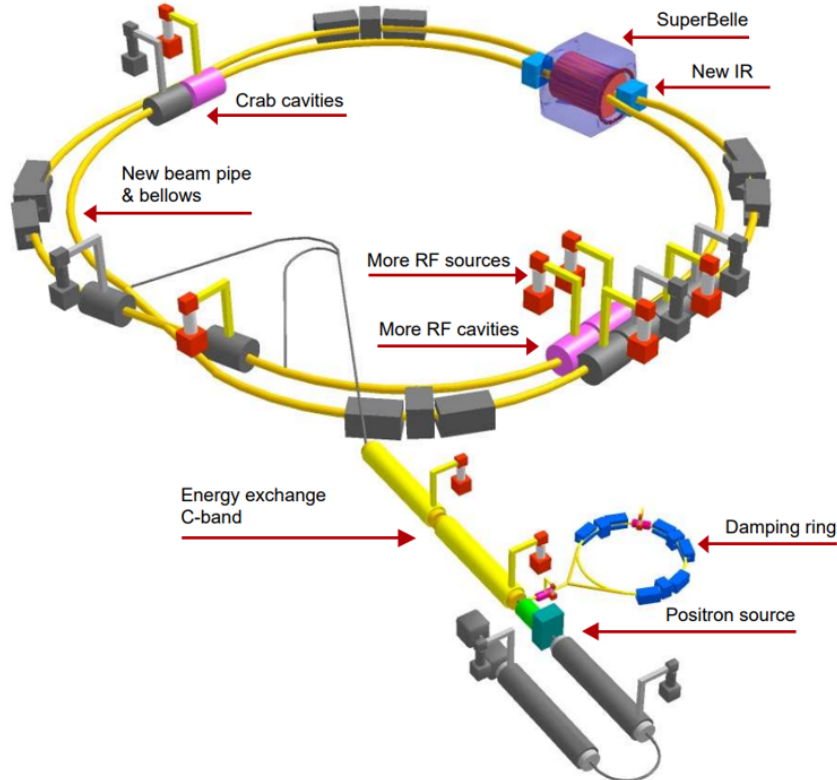


Figure 2.1: Schematic of the superKEKB accelerator.

smaller beam energy asymmetry (7 GeV on 4 GeV instead of 8.3 GeV on 3.5 GeV of KEKB), which reduces beam losses due to Touschek scattering in the LER, while reducing synchrotron radiation losses in the HER. This also improves the angular acceptance of the detector, making it useful to analyze events with large missing energy. The boost reduction, which reduces the average distance between the two B decay vertices, is compensated by an improved vertex detection.

To achieve the luminosity goal of SuperKEKB, two major upgrades are required: a two-fold increase in the beam currents and a significant reduction of the vertical beta function at the interaction point (β_y^*). The design of the beam parameters at SuperKEKB follows the “nano-beam” scheme, where each particle in a bunch interacts with only a small portion of the other colliding bunch. To increase the luminosity, a reduction of the interaction region of the colliding beams is also necessary. This restricts the vertex position along the beam axis and thus represents an additional benefit for more precise estimations of the primary vertex.

The choice of the main parameters of the accelerator, the beam energies and

the luminosity are shown in Table 2.1.

		Low Energy Ring (e^+)	High Energy Ring (e^-)	Units
Beam Energy	E	4	7	GeV
Beam Current	I	3.60	2.62	A
Half crossing angle	ϕ		41.5	mrad
Vertical beta function	β_y^*		0.4	mm
Luminosity	\mathcal{L}		8×10^{35}	$\text{cm}^{-2}\text{s}^{-1}$

Table 2.1: Main design parameters of the SuperKEKB accelerator.

The Belle II detector will be taking data with a 40 times higher instantaneous luminosity. A conservative factor of 10 to 20 increase is expected in the background hit rate, while physics event rate are expected to be about 50 times higher [25]. For the Belle II detector the main concern is to maintain the excellent performance of Belle even with higher background levels, which led, among the other things, to an increase in radiation damage and to fake hits in the electromagnetic calorimeter.

Figure 2.2 shows a sketch of the detector with its coordinate system, which is centered at the beam interaction point.

2.2 VERTEX DETECTOR

The main purpose of the Vertex Detector (VXD), together with the CDC, is to give precise measurements of the decay vertices. It comprises altogether six layers located around a 10 mm radius Beryllium beam pipe. The first two layers, at $r = 14$ mm and $r = 22$ mm, uses pixelated sensors of the DEPFET type, that constitute the PXD. The remaining four layers, at radii $r = 38$ mm, 80 mm, 115 mm and 140 mm are equipped with double-sided silicon strip sensors. The complex of these four layers constitute the SVD.

2.2.1 PIXEL VERTEX DETECTOR

Detectors like the PXD, so close to the beam pipe, deal with high hit rates, caused mostly by beam-related background. Thus, the layers of a high precision vertex detector cannot be realized by strip detectors, due to the large occupancy

2.2. VERTEX DETECTOR

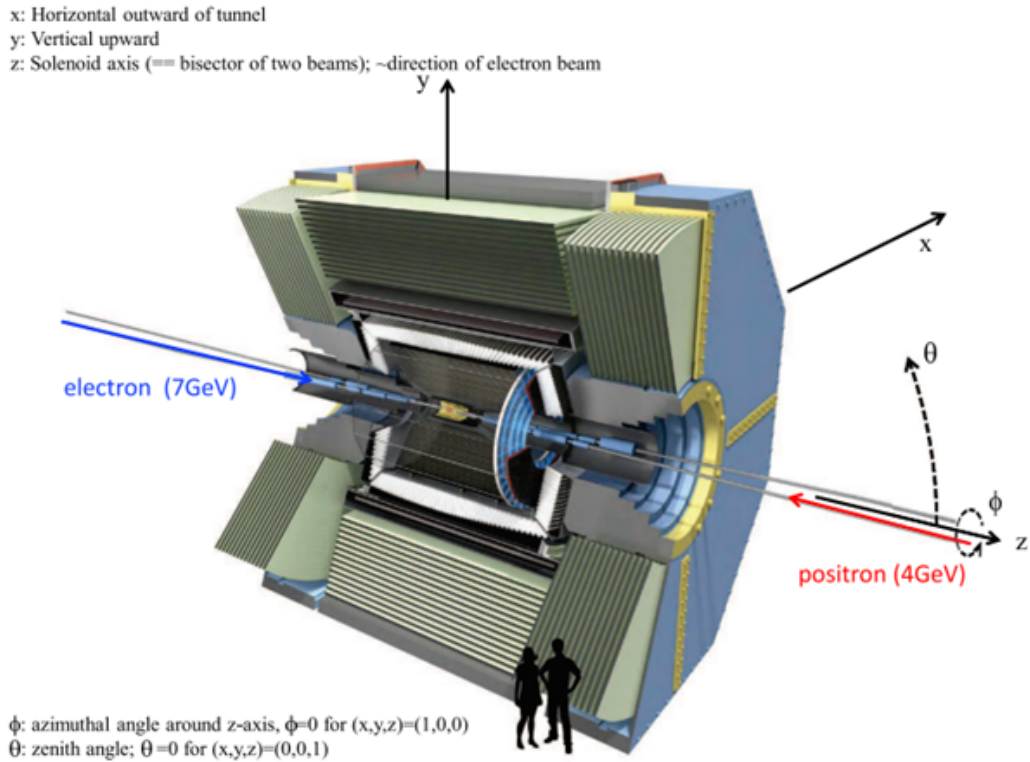


Figure 2.2: 3D representation of the Belle II detector. The x coordinate is directed opposite compared to the center of the accelerator, the y coordinate is directed upward and the z coordinate is the bisector of the two beams and is directed towards the forward region. The θ angle is the polar angle and $\theta = 0$ for $(x, y, z) = (0, 0, 1)$, while ϕ is the azimuthal angle and ϕ for $(x, y, z) = (1, 0, 0)$ [26].

(defined as the fraction of channels hit in each triggered event) they would deal with. Consequently, pixel sensors are used, rather than strips, for the innermost layers, having a much larger number of channels and therefore a much smaller occupancy.

The PXD is a barrel system consisting of two cylindrical layers of active pixel sensors, see Figure 2.3. The inner layer is made of 8 planar sensors (ladder), each with a width of 15 mm and a sensitive length of 90 mm. The outer layer consists of 12 modules with a width of 15 mm and a sensitive length of 15 mm. In each layer the sensitive lengths are determined by the required angular acceptance of the tracking system: a polar angle range from 17° , for the forward direction, to 150° , for the backward. The asymmetry in the angular range is to account for the forward boost of the centre-of-mass frame.

The PXD is composed of around 8 million pixels in total. In order to improve

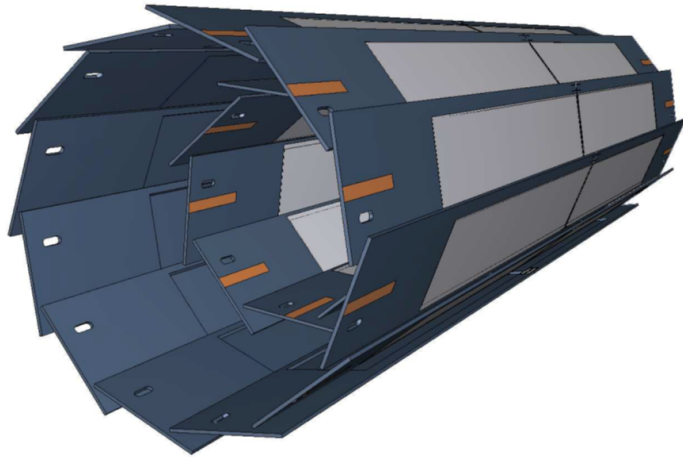


Figure 2.3: The geometrical arrangement of the two layers of sensors for the PXD. The light grey surfaces are the DEPFET pixels.

the resolution on the position of individual hits, which is limited by multiple scattering, a very thin technology is required: the sensitive area of each PXD sensor is $75\ \mu\text{m}$ thick. The size of the pixel surface is $50 \times 50\ \mu\text{m}^2$ and $50 \times 75\ \mu\text{m}^2$, respectively, in the innermost and outermost layers. These sizes are determined by the requirements on the vertex resolution, that should be better than $20\ \mu\text{m}$.

The PXD sensors are based on the DEPFET (DEPleted Field Effect Transistor) technology. A DEPFET device is a semiconductor-based device that detects and amplifies signals. This makes the DEPFET technology excellent to minimize the material budget.

2.2.2 SILICON VERTEX DETECTOR

The design of the SVD consists of four layers, labeled from 3 to 6, of doubled-sided silicon strip detectors (DSSDs). Each layer consists of a different number of modules, called ladders, arranged around the interaction point in the typical cylindrical geometry. Ladders are equipped with three different kind of sensors: ladders of layer 3 consists of two equal rectangular sensors of size $123\ \text{mm} \times 38\ \text{mm}$, while the ladders of layers 4, 5 and 6 have, respectively, 2, 3 and 4 rectangular sensors of size $123\ \text{mm} \times 58\ \text{mm}$ and one trapezoidal sensor in the forward region.

The larger radius of the Belle II vertex detector, compared to that of Belle, would require an increase in the number of wafers and, thus, in the material budget. Thus, trapezoidal sensors in the forward region are slanted of an

2.2. VERTEX DETECTOR

appropriate angle with respect to the other sensors, as displayed in Figure 2.4. This arrangement aims also to improve the angular acceptance and optimize the incident angle on the sensor of particles coming from the interaction point.

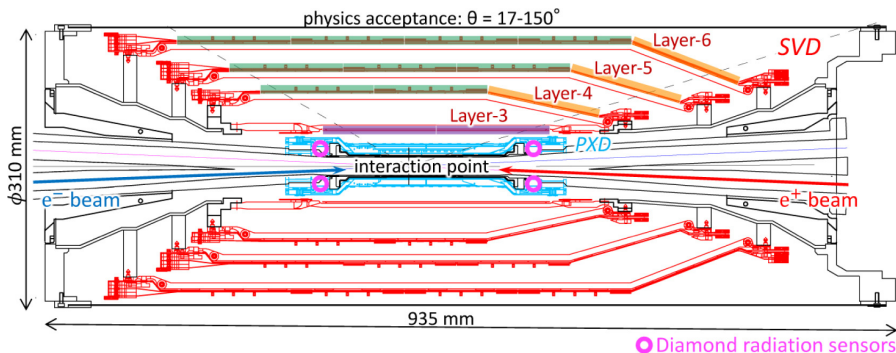


Figure 2.4: Side view of the SVD layers showing the different sensor composition. Orange lines are the slanted sensors in the forward region of layers 4,5,6. Green and violet lines are the rectangular sensors in the barrel region.

The polar angular acceptance of the SVD, from 17° to 150° , covers the full Belle II coverage, the same as the PXD and CDC.

All the rectangular silicon sensors are double-sided, with the long p-side strip parallel and facing the beam axis z and the short n-side strip along the $r - \phi$ plane, located towards the outside.

The SVD is used in conjunction with the drift chamber to improve the quality of the track parameters, but is also used for stand alone, which is important for the reconstruction of low momentum particles.

WORKING PRINCIPLE OF SVD

The main purpose of the SVD, together with the PXD, is the extremely precise measurement of the tracks near the interaction point and the reconstruction of the decay vertices of B mesons, D mesons and τ leptons. To the reconstruction of tracks with low transverse momentum, which can be affected particularly by multiple scattering, DSSD sensors are required, since they provide a very precise measurement of the position of charged particles on sensors. DSSD sensors are based on the working principle of p-n junctions.

In the DSSD sensors adopted for the Belle II SVD, an asymmetric p-n junction is based on a highly p-doped semiconductor and on a n-doped substrate, called bulk. When a charged particle crosses the sensor, a electron-holes (e-h) pair is generated. A bias voltage, V_b , makes the e-h pairs towards the electrodes of the

sensors. The motion of the charge carriers generates an electric current on the electrodes that is the signal of response of the sensor at the passage of the particle. The electrodes provide also spatial information about the passage of the particle: sensor elements closest to the crossing point of the particle with the sensor will collect most of the induced signal (with respect to the other neighboring sensor elements). For this reason, the SVD sensors are segmented with long, thin sensor elements called *strips* that extend the full length, and width, of the sensor. Usually, strips are a few tens of μm wide. They can be spaced by a few tens of μm to hundreds of μm distance: the separation between strips is called *pitch*. The strips allow to measure the position of the crossing ionizing particle, providing a one-dimensional measurement of its position. Since the electrodes are segmented in both sides of the sensor, a two-dimensional measurement of the position is achievable by the Belle II DSSD: p^+ strips are implemented on one side and, orthogonally, n^+ strips are implemented on the opposite side of the sensor. Aluminium strips are used for the readout of electrode strips and are isolated from the silicon substrate by a SiO_2 layer. This layer contains positive oxide charges, trapped in the oxide layer at the moment of the fabrication. The positive oxide charge attracts electrons generating an accumulation region. Electrons form a layer of negative charge that reduces the n-doped electrode strips. This accumulation region can be interrupted introducing p-doped strips, called *p-stops*, between the n^+ strips: p-stops strips introduce p-n junctions that drives the electrons away from the accumulation region. Figure 2.5 shows a schematic of the working principle of the DSSD sensor.

The p^+ strips are parallel to the z axis, so they measure the $r - \phi$ coordinate, while n^+ strips, perpendicular to the z axis, measure the z coordinate. The position of the particle crossing the sensor, x_p , is calculated by the weighted mean of the position of the strips where the signal is induced (the weights are the intensity of the signals induced on the individual strip). If the signal is induced on one single strip, the resolution on the position is $\sigma_{x_p} = d_{pitch}/\sqrt{12}$, where d_{pitch} is the value of the pitch. If the signal is induced on more strips, forming a cluster, σ_{x_p} is determined by the Signal-to-Noise-Ratio and by d_{pitch} .

2.3. CENTRAL DRIFT CHAMBER

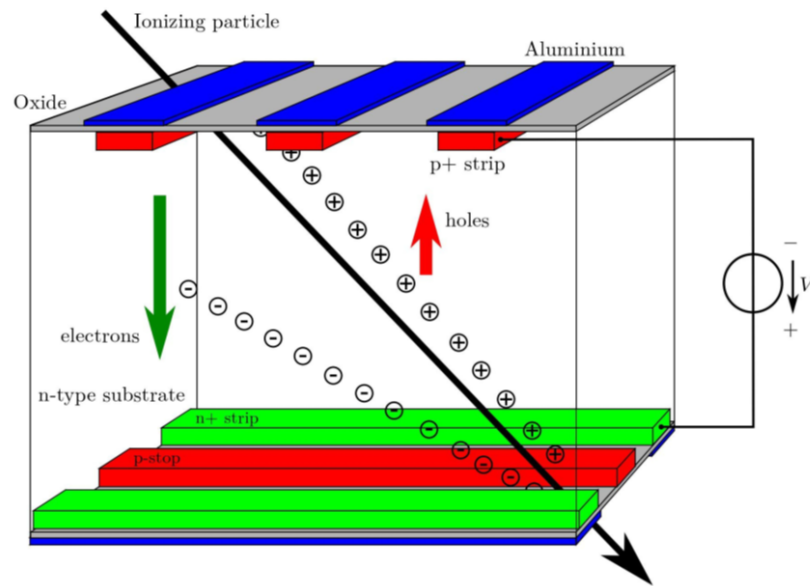


Figure 2.5: Schematic of the working principle of a DSSD device [27].

2.3 CENTRAL DRIFT CHAMBER

The central tracking device of the Belle II detector is a large volume drift chamber, with smaller drift cells than in Belle, so as to be able to operate at higher event rates with increased background levels. It starts just outside the SVD and extends to a larger radius (1130 mm compared to 880 mm of Belle).

The Central Drift Chamber (CDC) aims at reconstructing the trajectories of charged particles by precise measurements of charged particles momenta. It also provides particle identification (PID) through the information about the particle energy loss, dE/dx , within its gas volume. Similarly to Belle, the gas is a 50% helium 50% ethane mixture.

The chamber is made of 56 layers of wires divided in 9 superlayers with axial-stereo readout. The first 8 layers mount small cell (6-8 mm), whereas the other 48 layers mount bigger cell (10-18 mm), as shown in the top of Figure 2.6. The 9 superlayers and the configuration of the wires is shown in Figure 2.6 (bottom), where the axial and the stereo wires are represented respectively as blue and red dots.

Wires are similar to the Belle CDC: anode and cathode wires are gold-plated tungsten of 30 μ m diameter. The largest number of sensitive wires in the Belle II CDC allows to have a better granularity and a better spatial resolution on tracks.

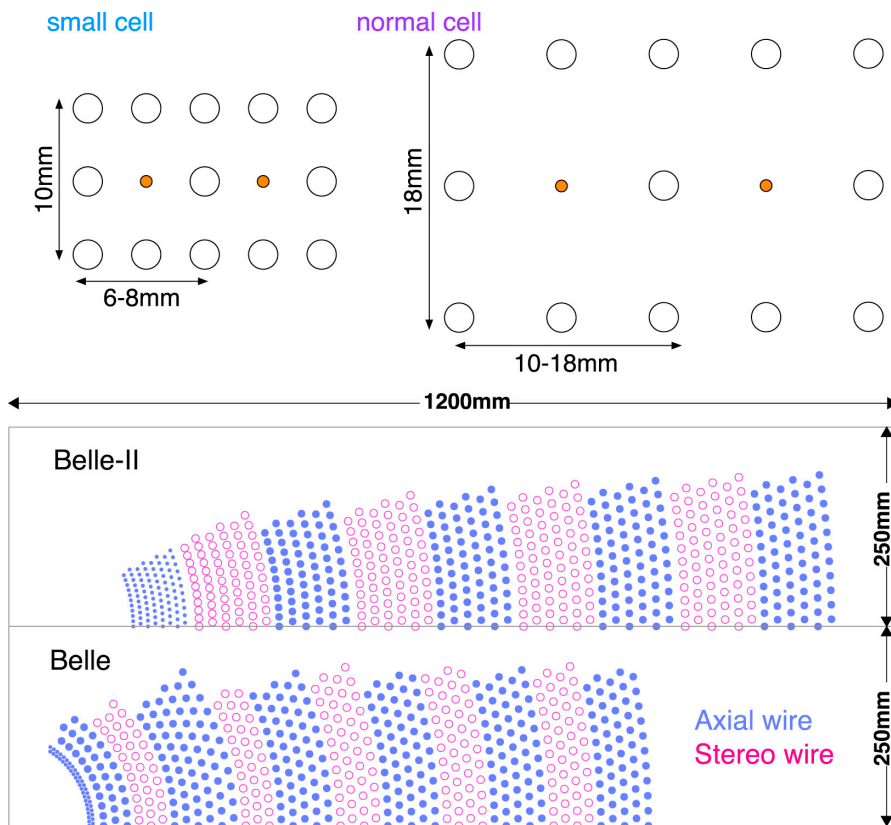


Figure 2.6: CDC cell dimensions (top). Comparison between the wire configuration in the CDC for Belle and Belle II (bottom) [25].

2.4. PARTICLE IDENTIFICATION SYSTEM

Compared to the Belle CDC, the Belle II CDC must face higher levels of background and a higher trigger rate. The total length of the chamber is 2.3 m. With respect to its predecessor, the Belle II CDC is enlarged. The higher inner radius allows also to avoid the high radiation levels near the IP. The measured spatial resolution on the individual hit is around $100 \mu\text{m}$.

2.4 PARTICLE IDENTIFICATION SYSTEM

In order to improve particle identification and, in particular, the K/π separation capability, Cherenkov detector are exploited in the Belle II detector. The PID system in Belle II is equipped with Time Of Propagation counter (TOP) and Aerogel Ring Imaging Cherenkov detector (ARICH).

2.4.1 TIME OF PROPAGATION COUNTER

The TOP counter is located in the barrel region of the Belle II detector, between the electromagnetic calorimeter inner support and the CDC outer cover. It is made of 16 modules arranged around the CDC on a radius of 1.24 m length.

Each module is made of quartz bar of $2.7 \text{ m} \times 45 \text{ m} \times 2 \text{ m}$ dimensions. The TOP measures the time of propagation of the Cherenkov photons propagating into the quartz radiator bars. The radiators are equipped with micro-channel plate photomultipliers (MCP-PMTs) located at one of the final parts of the bars and by a spherical focusing mirror on the other part of the bar. The spherical mirror aims to reduce chromatic errors, avoiding the dispersion of photons.

When crossing the quartz bar, particles produce Cherenkov photons that are propagated on the inner walls of the radiator. The direction of the Cherenkov photons, respect to the direction of the particle momenta, is defined by the Cherenkov angle θ_C , that will characterize the Cherenkov ring image: it is the total reflection on the inner walls that allows to preserve the Cherenkov ring image. The Cherenkov photons are then focused towards the MCP-PMTs by the focusing mirror. Between the quartz bar and the MCP-PMTs, an expansion prism is installed with the aim to expand the Cherenkov ring image.

Finally, a measurement of the time of propagation, t_{TOP} , of the Cherenkov photons is performed by the MCP-PMTs, that provide also informations about the arrival (x, y) coordinates of the photons. A 3-dimensional information, (x, y, t_{TOP}) , provided by the same MCP-PMTs allows to reconstruct the Cherenkov

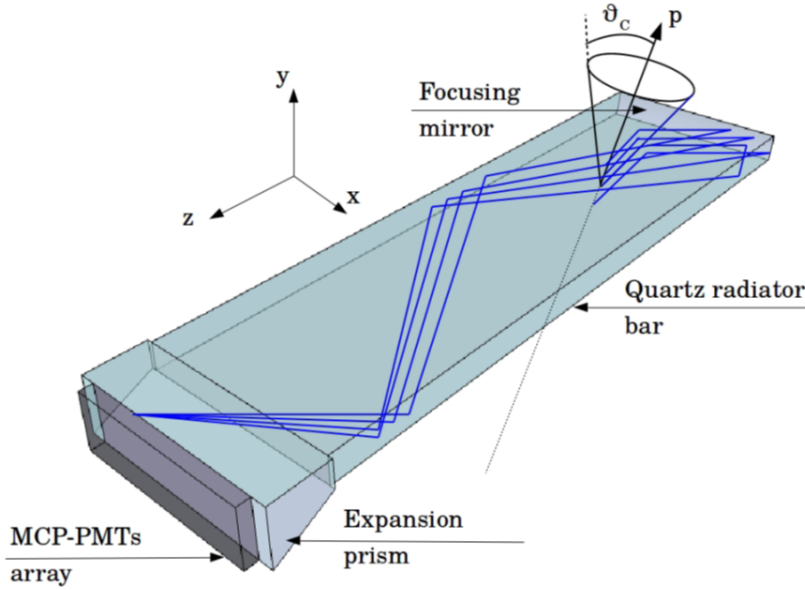


Figure 2.7: Schematic view of the TOP counter, with its main components: the quartz bar, the MCP photomultipliers and the expansion prism. Blue lines represent the direction of Cherenkov photons [25].

ring image.

Figure 2.7 shows a schematic view of the TOP detector.

The detected photons are also used to evaluate the K/π separation. Probability density functions (PDFs) are assigned for each particle hypothesis ($\mathcal{P}^K(x, t)$ and $\mathcal{P}^\pi(x, t)$) based on single tracks momentum, impact position, and angle on the quartz bar. Then, the photons detected for each track by the MCP-PMTs are tested against this two PDFs hypothesis. A likelihood function is determined for a simulated charged particle and defined as:

$$\mathcal{L}^{K,\pi} = \prod_i \mathcal{P}_i^{K,\pi}(x, t) \quad (2.1)$$

where the index i runs over the detected photons. Given the quantity,

$$\Delta \log \mathcal{L} = \log \mathcal{L}^\pi - \log \mathcal{L}^K, \quad (2.2)$$

if the log-likelihood is positive, the particle is classified as a pion, otherwise as a kaon.

Figure 2.8 shows a typical example of the log-likelihood distribution.

2.4. PARTICLE IDENTIFICATION SYSTEM

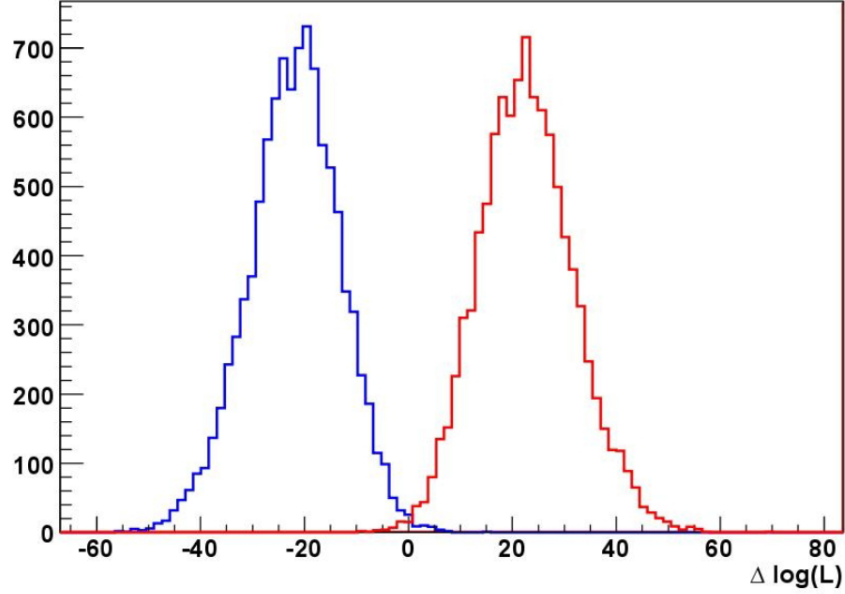


Figure 2.8: Distribution of $\Delta \log \mathcal{L}$ for π (red) and K (blue) [25].

The TOP counter provides a time resolution lower than 50 ps.

2.4.2 AEROGEL RING-IMAGING CHERENKOV DETECTOR

The ARICH detector, placed in the forward region of the detector, is designed to improve the K/π separation for particles up to 4 GeV/c momenta and to distinguish between π, μ, e with momenta below 1 GeV/c.

The working principle of the ARICH is based on the aerogel radiator, in which charged particles produce Cherenkov photons that are then detected by dedicated photon detectors. A 20-cm-thick expansion volume is installed between the aerogel radiator and the array of photon detectors, in order to produce large enough Cherenkov rings.

The ARICH consists of two aerogel radiators, of equal thickness but different refractive index ($n_1 = 1.046$ for the first and $n_2 = 1.056$ for the second). The presence of the two aerogel radiators make the photon from the two radiators arrive in the same point of the focal plane, as shown schematically in Figure 2.9.

This increases the resolution in the measurement of the Cherenkov angle θ_C , without any penalty in the intensity of the light. In fact, the resolution on the Cherenkov angle for N photons detected is $\sigma_{\theta_C}^N = \sigma_{\theta_C} / \sqrt{N}$. For an individual

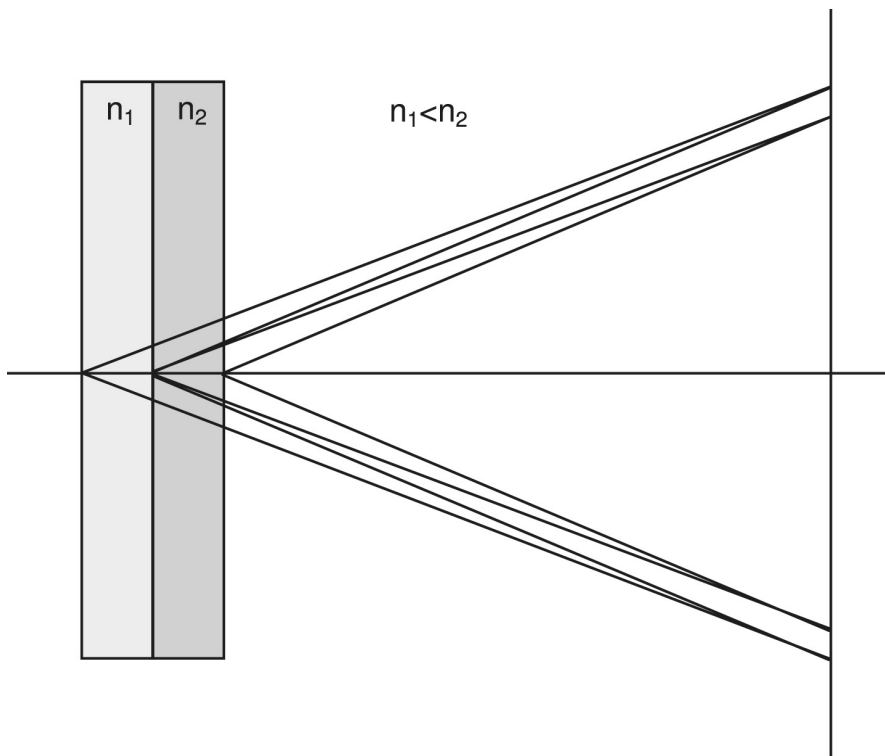


Figure 2.9: Schematic configuration of the ARICH [25].

photon $\sigma_{\theta_c} = 14 \text{ mrad}$, for an expected number of photons detected of about 20 for track, we have $\sigma_{\theta_c}^N \simeq 14 \text{ mrad}$.

Photon detectors are based on Hybrid Avalanche Photo-Detectors (HAPD) technology, that consists of a vacuum tube with solid state sensor of avalanche-diode type photo-detector (APD). HAPDs are arranged in 9 concentric rings and a total of 540 sensors of size $73 \text{ mm} \times 73 \text{ mm}$ are installed.

Cherenkov photons generate photoelectrons from a photocatode via photoelectric effect. Photoelectrons are then accelerated by a typical potential difference of 7-10 kV towards the APDs, which provide a gain of a factor 40.

With an inner radius of 410 mm and an outer radius of 1140 mm, the ARICH has a geometric acceptance from $\theta \simeq 15^\circ$ to $\theta \simeq 30^\circ$.

2.5 ELECTROMAGNETIC CALORIMETER

A high resolution calorimeter is an important part of the Belle II detector, since 1/3 of the B-decay products are neutral particles that provide photons in a $[20 \text{ MeV}, 4 \text{ GeV}]$ energy range. Among the main tasks of the electromagnetic

2.5. ELECTROMAGNETIC CALORIMETER

calorimeter there is the high efficiency in photons detection and photon energy, electron identification, K_L^0 detection together with the KLM and the generation of the signal for trigger.

The same material as Belle, CsI(Tl) crystals, has been chosen for the Belle II electromagnetic calorimeter (ECL). The Belle ECL consists of a 3 m long barrel section. It has an inner radius of 1.25 m and annular endcaps at $z = 1.96$ m, in the forward region, and $z = -1.02$ m, in the backward, from the interaction point. The angular polar region spans over $12.4^\circ < \theta < 155.1^\circ$, except for two gaps of about 1° wide between the barrel and endcaps.

The total amount of 8736 crystals are distributed as follows: 6624 in the barrel region and the remaining 2112 in the endcaps. The crystals in the barrel region are of 29 distinct shapes with sizes of about 6×6 cm² in cross section and 30 cm (equal to $16.1 X_0$) in length, those in the endcaps have up to 69 different shapes.

Due to the high background level, electronics based on waveform sampling with pipelined readout has been designed for the Belle II ECL. This allows to use time information to reject off-time events hits and to parallelize the readout processes, reducing dead times. For scintillation light readout, two 10×20 mm² photodiodes are glued to the surface of the crystal.

A preamplifier is connected to each photodiode, so as to have two independent output for each crystal. The two pulses are then added and processed by two different shaper boards: one shaper is used to generate the trigger signal, while the other produces the signal waveform that will be sampled and used to extract amplitude and timing informations. The output signal of the crystals, as measured through a calibration with cosmic ray muons, is about 5000 photoelectrons per MeV.

The energy resolution of the calorimeter, measured in a prototype, can be approximated as

$$\frac{\sigma_E}{E} = \sqrt{\left(\frac{0.066\%}{E}\right)^2 + \left(\frac{0.081\%}{\sqrt[4]{E}}\right)^2 + (1.34\%)^2} \quad (2.3)$$

where E is expressed in GeV and the first term represents the electronics noise contribution.

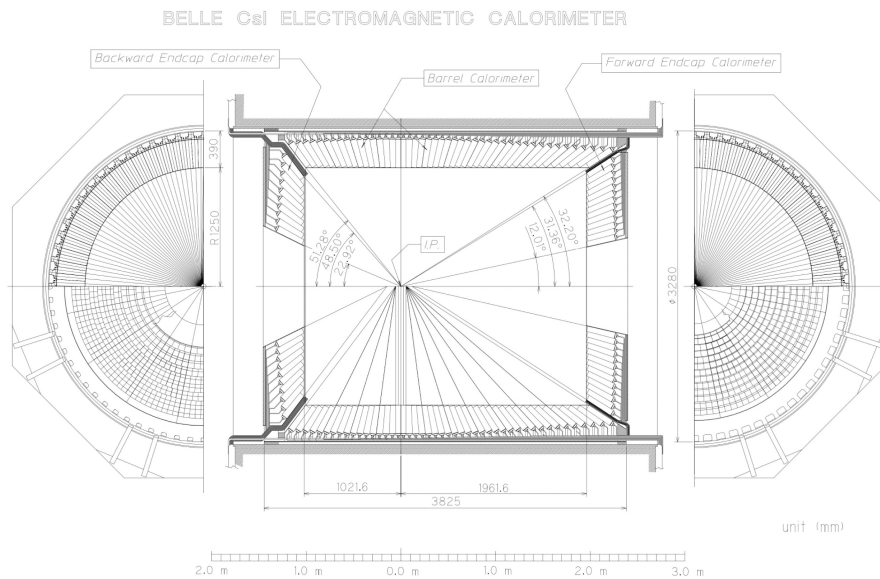


Figure 2.10: Schematic view of the ECL. The three detector regions, barrel, forward and backward end-caps, are shown. Image taken from [28].

2.6 KLM

The outermost sub-detector of Belle II is dedicated for the K_L^0 and μ reconstruction. It consists of an alternating 14-layer sandwich of iron plates and active detector elements installed outside the superconducting solenoid. The iron plates serve as the magnetic flux return for the solenoid and also provide $3.9 X_0$ or more of material in which K_L mesons can shower hadronically.

The octagonal barrel has a polar angle coverage from 45° to 125° , while the endcaps from 20° to 155° . There are a total of 15 detector layers and 14 iron plates in the barrel region and a total of 14 detector layers and 14 iron plates in each endcap. A side view of the KLM is shown in Figure 2.11.

The KLM is composed by glass-electrode resistive plate chambers (RPC), located in the outermost layers of the barrel region, and by scintillator strips coupled with silicon photomultiplier (SiPM), installed in the endcaps and in the two innermost layers of the barrel region. The RPCs are composed by two electrodes made by high resistivity glass spaced of 2 mm. This space is filled with a mixture of 62% HFC-134a freon, 30% argon and 8% butane. The outer surface of each electrode is covered with a carbon-doped paint that allows to distribute high voltages to electrodes.

A charged particle crossing the RPCs ionizes the gas molecules: the electric

2.6. KLM

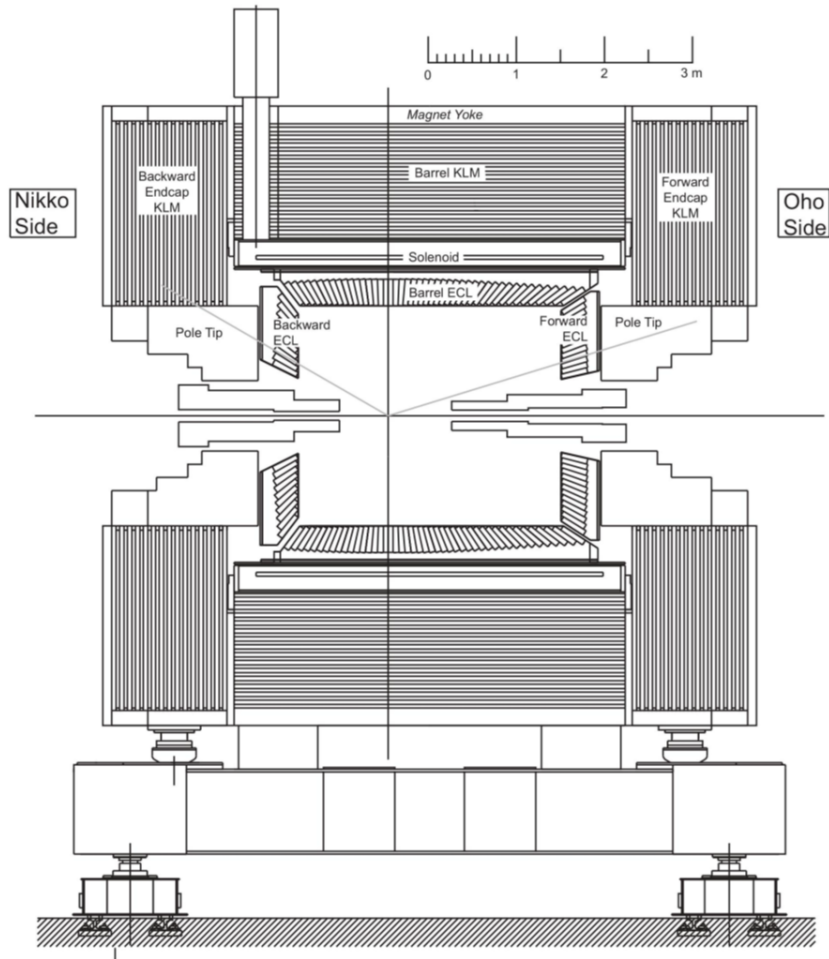


Figure 2.11: Side view of the KLM. Grey lines represent the nominal acceptance. Image taken from [25].

field accelerates the electrons towards the anode and ions towards the cathode. Electrons and ions induce a signal on a metal strips located on each side of RPCs. These metal strips are arranged orthogonally in order to measure both z direction and ϕ direction.

Because of the high rate environment of Belle II, endcaps of the KLM are equipped with scintillator strips that are coupled with SiPM for the signal read-out. Each strip has an optical fiber arranged in its centre. The fiber pick up the scintillation light and carries it to the SiPMs. This system of fibers coupled with SiPM is characterized by a high time resolution and by a high output rate capability.

2.6.1 MUON AND K_L IDENTIFICATION

Muons and non-showering charged hadrons traverse the KLM until they escape or range out due to electromagnetic energy deposition, depending on their momentum. Instead, K_L mesons create a hadronic shower that can be detected in either the ECL alone, the KLM alone, or both.

MUON IDENTIFICATION

Muon identification begins with the reconstruction of a charged track in the CDC. The track is extrapolated beyond the outermost CDC under a π -hypothesis. The track is thus considered within the KLM acceptance if it crosses at least one module: this requires a minimum momentum of 0.6 GeV. If a KLM hit is found near the crossing of the extrapolated track with a KLM layer, then the hit is associated with the track. The outermost layer crossed by the extrapolated track defines the *predicted range* of the track, while the *actual range* is determined by the outermost layer with an associated hit. If the predicted and the effective range differ significantly, the track is classified as hadron. Otherwise the same extrapolation is repeated starting from the extrapolation of the track, but assuming now a μ -hypothesis per the particle. The difference between the predicted range and measured range, as well as the goodness of fit of the transverse deviations of the associated hits from the re-extrapolated track, provide the two variables used to test the hypothesis that the track resembles a muon rather than a charged hadron.

K_L IDENTIFICATION

Hits that in the KLM are within a 5° opening angle (measured from the interaction point) of each other are grouped together into a cluster. After all clusters have been formed, a charged track veto is applied. Then a straight line is drawn between the track entrance point in the KLM and the interaction point. Two scenarios can occur. This line is within 15° of the line between the cluster centroid and the interaction point, thus the cluster is discarded. Or, the cluster is aligned with a reconstructed ECL cluster to within 15° , thus the ECL and KLM cluster are associated (in this case the ECLs cluster direction overrides that of the KLM). Finally, a cut on the cluster size is imposed: a K_L candidate is classified as a KLM-only candidate if the cluster have hits in at least two distinct layers;

2.7. TRIGGER SYSTEM

if the cluster have a hit in the ECL and at least one KLM hit it is classified as a KLM+ECL candidate.

2.7 TRIGGER SYSTEM

Belle II employs a two-level trigger system: the L1 is hardware-based, while the High Level Trigger is realized in a computer form. The requirements for a trigger system are a high efficiency for hadronic events from $B\bar{B}$ decays, a fixed latency of about $5\ \mu\text{s}$, a timing precision of less than $10\ \text{ns}$, a minimum two-event separation of $200\ \text{ns}$.

In the Belle II, the L1 trigger system consists of sub-trigger systems and one final-decision logic. A sub-trigger system summarizes the trigger information coming from its sub-system, and then sends the information to the final-decision logic. In the Belle II design, each component is equipped with a FPGA, so that the trigger logic is configurable.

Each sub-detector carries different informations:

- the CDC sub-trigger provides the charged track information (momentum, position, charge);
- the ECL sub-trigger gives energy deposit information, energy cluster information, Bhabha identification;
- the Barrel PID sub-trigger gives precise timing and hit topology information;
- the Endcap PID sub-trigger is expected to give precise timing information;
- the KLM sub-trigger gives muon track information;
- the Global Decision Logic (GDL) receives all of this sub-trigger information and makes the final decision.

The total latency of the L1 trigger is around $5\ \mu\text{s}$. The Trigger is affected by an uncertainty of around $10\ \text{ns}$ called trigger jitter (TJ).

2.7.1 HIGH LEVEL TRIGGER

The High Level Trigger (HLT) uses the full reconstruction of the event using the data coming from all sub-detectors. A software trigger for the event is produced using the physics event-selection software that is composed by two parts: the Level 3 Trigger (L3) and the physics-level event selection trigger.

After a fast track reconstruction and a fast reconstruction of the ECL clusters, the L3 gives a constraint on the track multiplicity, on the vertex position of the event and on the total energy deposit in the ECL. In this way, a reduction of 50% of data and of the processing time for each event are expected.

The physics-level event selection trigger performs the full event reconstruction. The event selection employs similar selection criteria used to produce skims, as for example the hadronic selection or the low-multiplicity selection. The total selection of the events that passes the L3 trigger is around 25%.

2.8 BELLE II SOFTWARE AND COMPUTING

The Belle II computing system is an infrastructure of many facilities distributed to all the members of the collaboration. The data taken are stored, the parameters dependent on the condition of the experiment are continuously determined and written in database. The raw data are processed in the high-level information and then saved. In addition to the real data, MC samples are produced and also stored.

The software framework used by the Belle II experiment is called Belle Analysis Framework 2, or more briefly *basf-2* [29], that is used both for online and offline data management, as for physics analysis or detector software optimizations.

Finally, the database contains the information about the geometry of the detector, the material budget of every single piece of the detector, the calibration constants, the accelerator parameters and all those information needed to perform simulation or reconstruction of data.

3

State of the art of the $\tau \rightarrow \ell\gamma$ search

A brief summary of some of the experimental searches of these decays is presented in the following, with a specific focus on the $\tau \rightarrow \ell\gamma$ decay, that is regarded to be a golden mode for exploring New Physics scenarios. Up to now, the B-factories are the experiments that set the best upper limits to the $\tau \rightarrow \ell\gamma$ search: a detailed description of their analysis will be presented in the last section of this chapter.

3.1 LEPTON FLAVOR VIOLATING τ DECAYS

Many searches for neutrinoless decay have been made for many LFV τ decay modes, in particular:

- radiative modes: $\tau \rightarrow \ell\gamma$, where $\ell = \mu, e$;
- three lepton modes: $\tau \rightarrow eee, \tau \rightarrow e\mu\mu, \tau \rightarrow \mu\mu\mu, \tau \rightarrow \mu ee$;
- semi-leptonic modes: $\tau \rightarrow \ell h^0, \tau \rightarrow \ell h^+ h^-$, where h^0 can be a scalar, pseudo-scalar or vectorial neutral hadron, $h = K, \pi$ and $\ell = \mu, e$;
- hadronic modes: $\tau \rightarrow \Lambda h$, where $h = K, \pi$.

Over the years, no evidence of a signal has been found for lepton flavor violation, allowing physicists to set upper limits on the branching ratios of these decays. Figure 3.1 illustrates the limits set on different LFV decays at the 90% CL by the CLEO, BaBar, Belle and LHCb experiments. In the same figure, red dots represent the future prospects for the Belle II experiment with a data sample equal to 50 ab^{-1} .

3.2. BRIEF HISTORY OF THE LFV SEARCHES

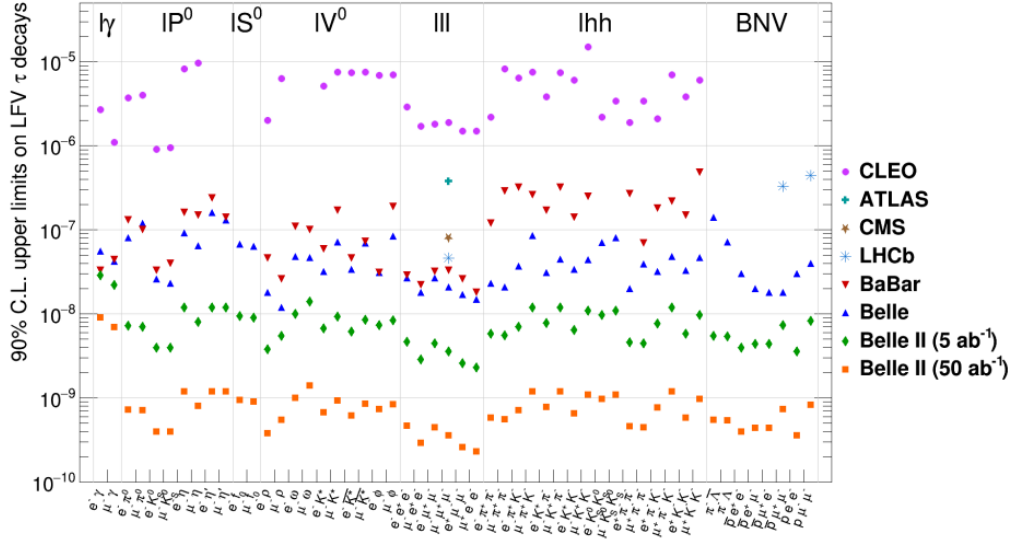


Figure 3.1: 90% C.L. upper limits for the LFV τ decays. Results come from the CLEO, ATLAS, CMS, LHCb, BaBar and Belle collaborations. Green and orange dots represent the projections for the Belle II experiment, based on the current Belle analysis, assuming $\mathcal{L}_{int} = 5 \text{ ab}^{-1}$ and 50 ab^{-1} respectively. Image taken from [30].

3.2 BRIEF HISTORY OF THE LFV SEARCHES

Lepton flavour violating neutrinoless τ decays have been studied extensively in the last decades. The first experimental result for the $\tau \rightarrow \ell\gamma$ search has been reported, in 1982, by the Mark II experiment. With a magnetic detector, used to acquire about 17 nb^{-1} of data at the SPEAR electron-positron collider, with a CM energy between 3.58 and 6.85 GeV, the upper limits $BR(\tau \rightarrow e\gamma) < 6.4 \times 10^{-4}$ and $BR(\tau \rightarrow \mu\gamma) < 5.5 \times 10^{-4}$ [31] were set.

Further improvements to these measurements came few years later from the CLEO experiment at the CESR collider, that improved the search sensitivity to 2.73×10^{-6} for the electron channel [32] and to 1.1×10^{-6} for the muon channel [33]. CLEO analysis used data from the reaction $e^+e^- \rightarrow \tau^+\tau^-$ at or near the energy of the $\Upsilon(4S)$ resonance and corresponding to a total integrated luminosity of 4.68 fb^{-1} . Both the experiments searched for events in which the signal candidate τ decays into $e\gamma$ or $\mu\gamma$ and the other τ undergoes all standard tau decays into exactly one charged particle, any number of photon and at least one neutrino.

In the recent years, two different B-factories, BaBar and Belle, improved the results for the $\tau \rightarrow \ell\gamma$ search, setting the most stringent limits, respectively, to $BR(\tau \rightarrow e\gamma) < 3.3 \times 10^{-8}$ [34] and to $BR(\tau \rightarrow \mu\gamma) < 4.2 \times 10^{-8}$ [35]. Because of the importance of the results obtained, both the Belle and BaBar analysis will be treated in detail in the next section.

Figure 3.2 shows the improvements, over the years, in the search sensitivity for the $\tau \rightarrow \ell\gamma$ decay.

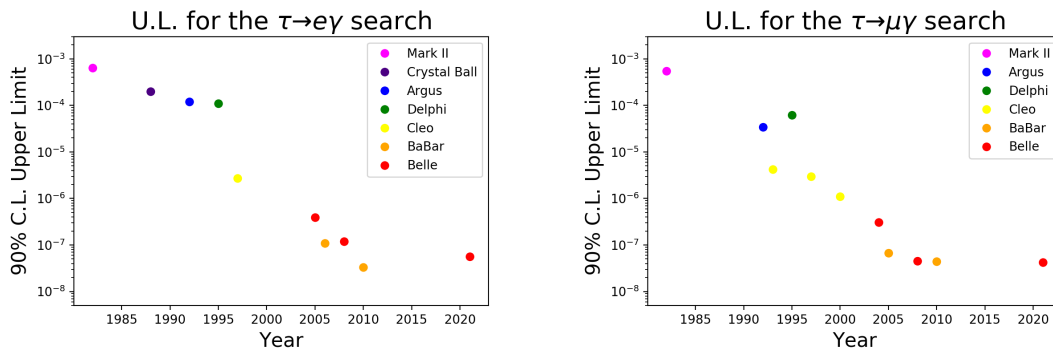


Figure 3.2: Trend of the sensitivity improvement for the $\tau \rightarrow e\gamma$ (left) and $\tau \rightarrow \mu\gamma$ (right) search.

All the previous measurements have been performed by experiments working with e^+e^- colliders, at different energies in the centre of mass. However, also at hadronic colliders it is possible to perform precision measurements on τ 's. The ATLAS, CMS and LHCb collaborations are examples of how this kind of searches can be performed with hadronic machines. The main result came from the LHC $\tau^\pm \rightarrow \mu^\pm\mu^+\mu^-$ search. This decay is of great interest for the study of charged LFV, since its final state, purely leptonic, is expected to be free of background. This allows to scale the experimental uncertainties linearly with luminosity and large sensitivity improvements can be expected with an increase of luminosity. The upper limit on the branching ratio set by the LHCb experiment is $\mathcal{B}(\tau \rightarrow 3\mu) < 4.6 \times 10^{-8}$ using 1.0 fb^{-1} data sample at 7 TeV and 2.0 fb^{-1} data sample at 8 TeV [36].

3.3 ANALYSIS TECHNIQUE AT THE B-FACTORIES

The analyses at the B-factories typically select τ -pair events from an e^+e^- collider. In the center-of-mass system (CMS), a candidate event is divided into

3.3. ANALYSIS TECHNIQUE AT THE B-FACTORIES

two hemispheres defined by the plane perpendicular to the thrust axis \hat{n}_{thrust} . This axis is defined such that the value

$$V_{thrust} = \frac{\sum_i \left| \vec{p}_i^{CMS} \cdot \hat{n}_{thrust} \right|}{\sum_i \vec{p}_i^{CMS}} \quad (3.1)$$

is maximized. Here, \vec{p}_i^{CMS} are the CMS momenta of each charged track and photon.

In the reconstruction of the event, each hemisphere contains either the τ^+ or τ^- decay products: the one containing the LFV $\tau^\pm \rightarrow \ell^\pm \gamma$ decay is referred to as *signal side*, while the other hemisphere, the *tag side*, includes the standard τ decays into one or more charged particles. As an example, the scheme of a candidate $\tau^+ \tau^-$ event is reported in the left side of figure 3.3: here, in the signal-side, one tau decays into $\tau^- \rightarrow \mu^- \gamma$, and in the tag-side, the other tau decays into one of the single charged decay modes $\tau^+ \rightarrow e^+ \nu_e \bar{\nu}_\tau$. The same figure shows, on the right, a simulation of how a similar event is recorded inside the BaBar detector.

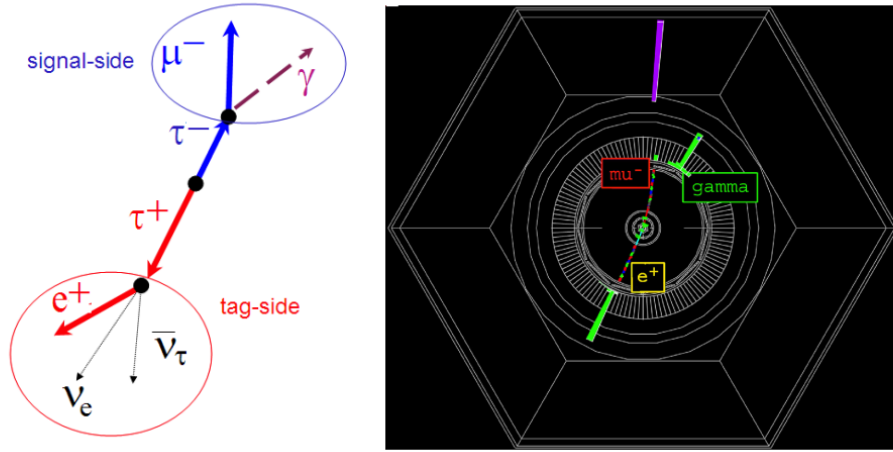


Figure 3.3: Scheme of a 1x1 topology event (left) with a LFV $\tau^- \rightarrow \mu^- \gamma$ decay and a SM one prong $\tau^+ \rightarrow e^+ \nu_e \bar{\nu}_\tau$ decay. On the right, its simulation for the BaBar detector.

The decay modes in which a τ decays into one charged particle are typically referred to as *one prong* decays and include the processes (and their charge

conjugates):

$$\tau^+ \rightarrow \mu^+ \nu_\mu \bar{\nu}_\tau$$

$$\tau^+ \rightarrow e^+ \nu_e \bar{\nu}_\tau$$

$$\tau^+ \rightarrow \pi^+ \bar{\nu}_\tau$$

$$\tau^+ \rightarrow \rho^+ \bar{\nu}_\tau.$$

Generally, events in which both the signal and the tag side present only one charged particle in each hemisphere are said to display a 1x1 topology.

Overall, the one prong decays constitute about the 85% of the τ decays, allowing to reconstruct a large fraction of the $\tau^+\tau^-$ produced and providing, thus, an analysis with high statistical power. This is the reason why this decay mode is widely used for the tagging of the event. Obviously, other different τ decay channels can be included among the tag modes, such as the *three prong* decays, in which the τ undergoes the SM decay:

$$\tau^+ \rightarrow \pi^+ \pi^- \pi^+ (\pi^0) \bar{\nu}_\tau$$

with three charged pions and, eventually, a π^0 . Candidate events with a three prong tag and a one prong signal are said to display a 3x1 topology.

While Standard Model τ decays have at least one neutrino, the $\tau \rightarrow \ell\gamma$ decay products have a well defined kinematics. In order to identify the LFV signal, two variables are typically used: the reconstructed mass of the decay products in the signal side, $m_{\ell\gamma}$, and the combined energy of the lepton and the photon, $E_{\ell\gamma}$. In the centre-of-mass system, $E_{\ell\gamma}$ is equal to the energy of the τ and it is approximately equal to the beam energy, $\sqrt{s}/2$, while, $m_{\ell\gamma}$ is equal to the mass of the τ . Using the set of variables

$$m_{\ell\gamma} = \sqrt{E_{\ell\gamma}^2 - p_{\ell\gamma}^2} \quad (3.2)$$

$$\Delta E = E_{\ell\gamma} - E_{beam}, \quad (3.3)$$

it is possible to separate the signal from the Standard Model τ decays background. In fact, the constraints $m_{\ell\gamma} = m_\tau = 1777 \text{ MeV}/c^2$ [37] and $\Delta E = 0$ serve as the most powerful requirement in the searches for LFV in τ decays.

The region encompassing events within approximately two standard deviations from $\Delta E = 0$ and $m_{\ell\gamma} = m_\tau$ is defined as the *signal region* into which the

3.3. ANALYSIS TECHNIQUE AT THE B-FACTORIES

analysis is then performed. Due to the correlation between the two variables, this region is described by a rotated ellipse in the $\Delta E - m_{\ell\gamma}$ plane. Figure 3.4 shows the distribution of a simulated $\tau \rightarrow \ell\gamma$ event in the Belle analysis. Shaded boxes represent the signal MC, solid circles the data and the inner dotted line delimits the 2σ signal region.

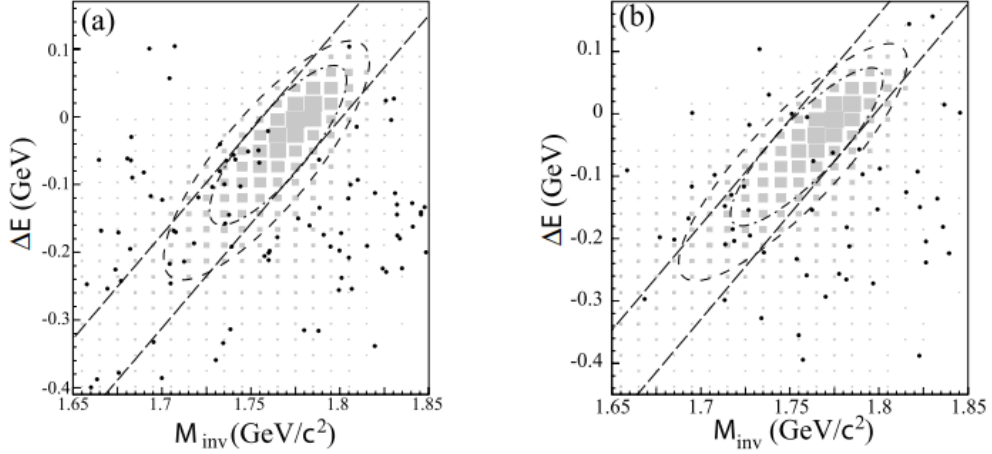


Figure 3.4: The distribution in the $\Delta E - m_{\ell\gamma}$ plane for (a) $\tau^\pm \rightarrow \mu^\pm\gamma$ and (b) $\tau^\pm \rightarrow e^\pm\gamma$ search in the Belle analysis. The solid circles and the shaded boxes show the data and the signal MC, respectively. The outer (inner) ellipse shows the 3 (2) σ signal region [38].

In the $\tau^\pm \rightarrow e^\pm\gamma / \mu^\pm\gamma$ search the dominant irreducible background comes from the radiative processes $e^+e^- \rightarrow e^+e^-\gamma / \mu^+\mu^-\gamma$. The remaining backgrounds come from τ pair events containing hard photon radiation and one of the τ leptons decaying to a charged lepton, and from hadronic τ decays where a pion is misidentified as the electron or muon.

In order to select the LFV $\tau \rightarrow \ell\gamma$ decay and suppress the background events produced in the e^+e^- collision, a selection is optimized using Monte Carlo simulation of signal and background samples. Signal efficiency (ϵ) is initially estimated using simulated events, while the estimate of the expected number of background events (N_{bkg}) is usually extracted from a maximum likelihood fit on the distributions of the Monte Carlo simulation of backgrounds.

The 90% C.L. branching ratio upper limit is calculated from:

$$BR(\tau \rightarrow \ell\gamma) < \frac{n_{signal}}{2 \cdot \epsilon \cdot \mathcal{L} \cdot \sigma(e^+e^- \rightarrow \tau^+\tau^-)} \quad (3.4)$$

where $N_{\tau\tau} = \mathcal{L} \cdot \sigma(e^+e^- \rightarrow \tau^+\tau^-)$ is the number of τ pairs produced in the e^+e^-

collisions with an integrated luminosity \mathcal{L} , given the τ pair production cross section σ .

Measurements such as that of a branching fraction or upper limit are performed at the B-factories using the method of the *blind analysis*, that aims at reducing the possibility of an experimental bias in a particular direction. The principle of a blind analysis is not to look at potential signal events, in a specific region, until most or all analysis criteria are finalized using data outside the signal region, MC simulations and/or control samples. This means that, in the BaBar and Belle analysis, there is no knowledge about the data in the signal region when optimizing for a best expected upper limit of the $\tau \rightarrow \ell\gamma$ search.

3.3.1 BABAR ANALYSIS

The BaBar experiment, operated between 1999 and 2008 at the SLAC National Accelerator Laboratory, was an asymmetric e^+e^- collider recording data at energies around the $\Upsilon(4S)$ resonance. The experiment made use of two accelerators to produce high energy particles: a linear accelerator (LINAC) to accelerate the electron/positron beams and the PEP-II storage rings facility. PEP-II consisted of two storage rings, the High Energy Ring (HER) for the 9.0 GeV electron beam and the Low Energy Ring (LER) for the 3.1 GeV positron beam. The two beams ran in opposite directions colliding at the Interaction Point (IP), where the detector registers the final state of the collision.

The BaBar detector was made up of a series of five subdetectors arranged cylindrically around the interaction point (IP). These are as follows, in order from inside to outside:

- Silicon Vertex Tracker (SVT) - provided precise position information on charged tracks recording particles tracks very close to the IP. Moreover, the SVT is the only sub-detector providing tracking measurements for low-momentum particles;
- Drift Chamber (DCH) - provided the momentum measurements for charged particles and participate in particle identification with dE/dx measurements;
- Detector of Internally Reflected Cerenkov radiation (DIRC) - radiate and focus Cerenkov radiation to provide charged hadron identification;
- Electromagnetic Calorimeter (EMC) - provided particle identification for electrons, neutral electromagnetic particles, and hadrons;

3.3. ANALYSIS TECHNIQUE AT THE B-FACTORIES

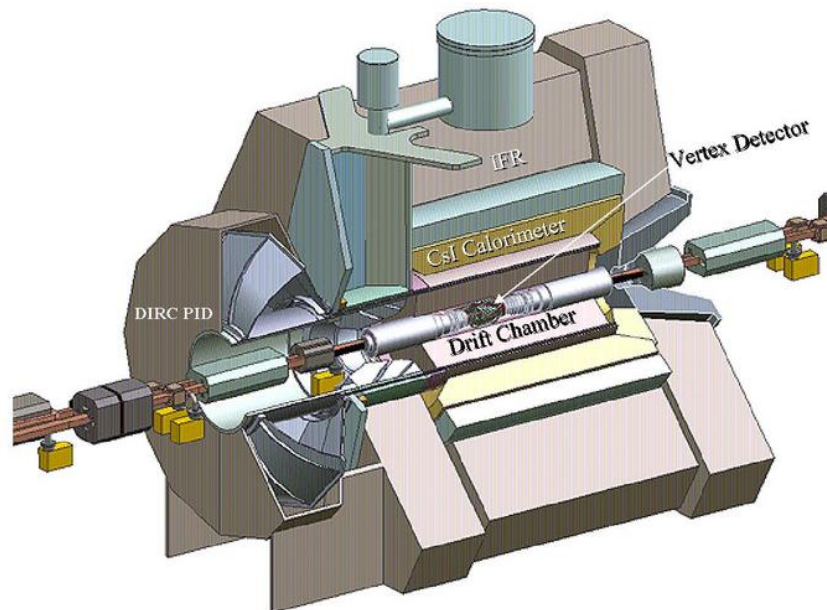


Figure 3.5: The BaBar detector.

- Instrumented Flux Return (IFR) - provides muon and neutral hadron identification.

A solenoid provided the 1.5 T magnetic field needed for charge and momentum measurements.

An illustration of the BaBar detector is reported in Figure 3.5.

Searches for LFV decays of a τ lepton to a lighter mass lepton and a photon have been performed with the entire dataset, corresponding to an integrated luminosity of 516 fb^{-1} , collected by the BaBar detector on and around the $\Upsilon(4S)$ resonances.

A candidate event must contain a τ pair, one reconstructed as decaying to one or three tracks, and the other as a $\ell\gamma$ pair. In the BaBar analysis, events with zero total charge and two or four well reconstructed tracks are selected, taking advantage of both the 1x1 and 3x1 topologies.

As regards the signal side, it must contain one track within the calorimeter acceptance and one photon whose origin is assigned to the point of closest approach of the lepton track to the e^+e^- collision axis. Kinematics considerations of two-body decays require that, in the CMS, the cosine of the opening angle between ℓ and γ must be less than 0.786.

The tag side is expected to contain a SM τ decay. A one prong tag is classified as

e -tag, μ -tag or π -tag if the track is identified, respectively, as an electron, a muon or a pion. If the track fails the lepton identification and the tag hemisphere contains a π^0 , reconstructed from a pair of photons with invariant mass between 90 and 165 MeV/ c^2 , the tag is classified as ρ -tag. A three prong tag is classified as $3h$ -tag if the hemisphere contains three charged tracks, all of which fail the lepton identification.

Different selection criteria are optimized, separately for the different tag decay modes, e -, μ -, π - and ρ -tag. Some of the variables used to develop the selection are the total CMS momentum of all tracks, the tag-side pseudomass [39] and the mass squared m_v^2 of the missing particles on the tag side. To further suppress the backgrounds, a neural net (NN) based discriminator is employed for each tag mode. This allows to improve the signal to background ratios for both the searches. These selections are optimized to yield the smallest expected upper limit for observing events inside a 2σ signal ellipse under background-only hypotheses.

The optimized selection leads to an efficiency in the reconstruction of the signal events equal to 3.9% for the $\tau \rightarrow e\gamma$ search and 6.1% for the $\tau \rightarrow \mu\gamma$. All contributions to the systematic uncertainties in the signal selection and reconstruction efficiencies are added in quadrature and amount to 7.7% for the $\tau^\pm \rightarrow e^\pm\gamma$ search and to 7.4% for the $\tau^\pm \rightarrow \mu^\pm\gamma$. The uncertainties include the photon reconstruction efficiency, the signal-lepton identification and track momentum, the signal-photon energy scale and resolution, trigger and filter efficiencies, tracking efficiency.

The analysis is blind in a 3σ ellipse in the $\Delta E - m_{EC}$ plane, where m_{EC} is the energy-constrained τ mass, obtained with a kinematic fit after requiring the CM τ energy to be $\sqrt{s}/2$ and after assigning the origin of the signal photon to the point of closest approach of the signal lepton track to the e^+e^- collision axis.

Outside the 3σ ellipse, a Fit Box (FB) is defined to extract the fractions of events for each type of background.

As shown in Figure 3.6, 0 and 2 events are observed for the $\tau \rightarrow e\gamma$ and $\tau \rightarrow \mu\gamma$ searches inside the 2σ signal ellipse. Thus, the frequentist upper limit for the branching ratios, calculated at the 90% C.L., are $\mathcal{B}(\tau^\pm \rightarrow e^\pm\gamma) < 3.3 \cdot 10^{-8}$ and $\mathcal{B}(\tau^\pm \rightarrow \mu^\pm\gamma) < 4.4 \cdot 10^{-8}$.

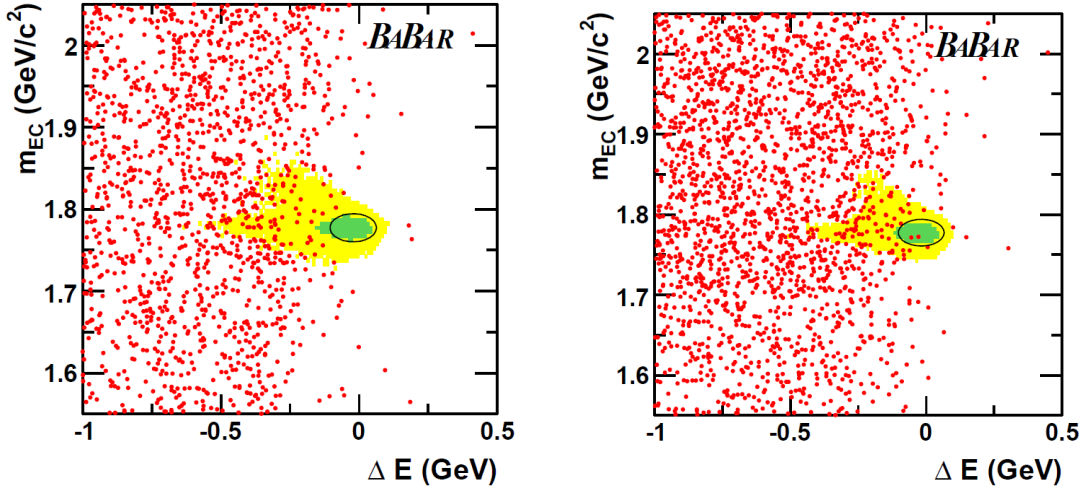


Figure 3.6: BaBar search for the $\tau^\pm \rightarrow e^\pm \gamma$ (left) and $\tau^\pm \rightarrow \mu^\pm \gamma$ (right) decay. In the $\Delta E - m_{EC}$ plane the black ellipse represents the 2σ signal region, data are shown as red dots and contours containing 90% (50%) of signal MC events are shown as yellow- (green-) regions. [40].

3.3.2 BELLE ANALYSIS

Belle was an experiment running at the KEKB e^+e^- asymmetric-energy collider, in Tsukuba, Japan. The experiment ran from 1999 to 2010 and collected a total amount of 988 fb^{-1} of data at energies of various Υ resonances in the centre of mass.

With its large solid angle coverage, the Belle detector collected data from 8 GeV electrons and 3.5 GeV positrons collisions. Belle consisted of a series of sub-detectors, among which:

- Silicon Vertex Detector (SVD) - provided for vertices measurements;
- Central Drift Chamber (CDC) - provided for charged particle tracking;
- Aerogel Cherenkov Counters (ACC) and time-of-flight scintillators counters (TOF) - together with the CDC informations, provided for particle identification by dE/dx measurements;
- Electromagnetic Calorimeter (ECL) - with an array of CsI(Tl) crystals detected electromagnetic showers;
- KLM - identified muons and K_L mesons.

A superconducting solenoid coil provided a 1.5 T magnetic field. Figure 3.7 shows a scheme of the Belle detector.

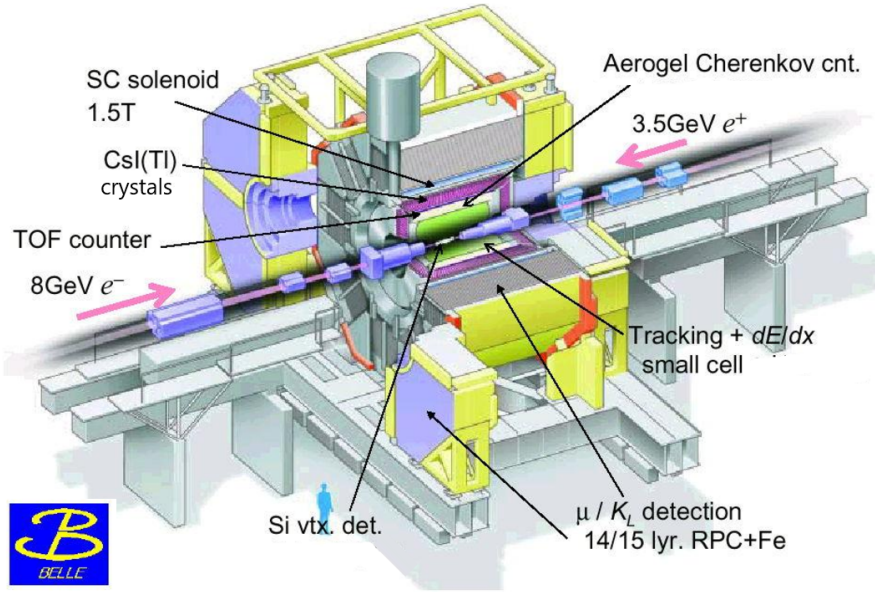


Figure 3.7: The Belle detector

The Belle analysis used the entire dataset, corresponding to 912×10^6 tau pairs. Since tau pairs are produced via $e^+e^- \rightarrow \tau^+\tau^-$ process, all the $\Upsilon(nS)$ resonances data have been used.

Belle searched for candidate events with exactly two oppositely charged tracks, in order to make the event's net charge zero. The signal-side tau decays to an electron (muon) and a photon for the $\tau^\pm \rightarrow e^\pm\gamma$ ($\tau^\pm \rightarrow \mu^\pm\gamma$) search: only one photon is required in this hemisphere, which must have $E_\gamma > 0.5 \text{ GeV}$. The tag-side tau is assumed to undergo one-prong decays, such as $\tau \rightarrow e\nu\bar{\nu}$, $\mu\nu\bar{\nu}$, $\pi\nu$, $\rho\nu$. In order to reduce the $e^+e^-\gamma$ ($\mu^+\mu^-\gamma$) contamination, an extra electron (muon) is vetoed in the tag-side using the criterion $\mathcal{L}_e < 0.1$ ($\mathcal{L}_\mu < 0.1$), for the $\tau \rightarrow e\gamma$ ($\tau \rightarrow \mu\gamma$) search. Here, \mathcal{L}_e (\mathcal{L}_μ) is the likelihood ratio used to identify electron (muon) candidates.

Kinematics considerations on two body decays require that the cosine of the angle between the lepton and the photon is less than 0.8. A further constraints is imposed to the overall cut $0.4 < \cos\theta_{\ell\gamma}^{CMS} < 0.8$.

After preselecting events, other selection criteria are applied to further suppress background events. Requirements on the total visible energy in the CMS, E_{total}^{CMS}/\sqrt{s} , are applied to suppress $e^+e^-\gamma$ and $\mu^+\mu^-\gamma$ events. Here, the visible energy is defined as the sum of the energies of all tracks and photons. The quantitative criteria are different for each of the tag decay modes, since the energy of the neutrinos is different for these channels.

3.3. ANALYSIS TECHNIQUE AT THE B-FACTORIES

The missing-mass-squared variable, m_ν^2 , is defined on the tag-side such that $m_\nu^2 = (E_{\ell\gamma}^{CMS} - E_{tag}^{CMS})^2 - |\vec{p}_{miss}^{CMS}|^2$. Here, $E_{\ell\gamma}^{CMS}$ (E_{tag}^{CMS}) is the sum of the energy of the signal (tag) side in the CMS and $|\vec{p}_{miss}^{CMS}|$ is the missing momentum, calculated by subtracting the sum of the three-momenta of all charged tracks and photons from the sum of the beam momenta. The signal distribution for m_ν^2 is distinct from $\tau^+\tau^-$ background due to kinematic difference and specific requirements are applied to suppress this specific background. Table 3.1 reports, for each specific tag channel, the selection criteria for the E_{total}^{CMS}/\sqrt{s} and m_ν^2 variables.

Tag mode	Visible energy [GeV]	Missing mass [GeV^2/c^4]
leptonic-tag	$E_{total}^{CMS}/\sqrt{s} < 0.93$	$0.0 < m_\nu^2 < 2.8$
π -tag	$E_{total}^{CMS}/\sqrt{s} < 0.86$	$-0.1 < m_\nu^2 < 1.2$
ρ -tag	$E_{total}^{CMS}/\sqrt{s} < 0.94$	$-0.3 < m_\nu^2 < 1.5$

Table 3.1: The selection criteria for the E_{total}^{CMS} and m_ν^2 variables.

To improve the search sensitivity, another variable is introduced, the energy asymmetry between the lepton and the photon in the signal side

$$\frac{|E_\ell^{CMS} - E_\gamma^{CMS}|}{(E_\ell^{CMS} + E_\gamma^{CMS})}. \quad (3.5)$$

The signal events are two-body decays, while the main background arises from three-body decays, $\tau^\pm \rightarrow \ell^\pm \nu_\ell \nu \tau$. The energy asymmetry should be larger in background events, thus the requirement $|E_\ell^{CMS} - E_\gamma^{CMS}|/(E_\ell^{CMS} + E_\gamma^{CMS}) < 0.65$ is applied to suppress them.

Two kinematic variables are adopted to select signal events: the beam-constrained mass, M_{bc} , and the normalized energy difference, $\Delta E/\sqrt{s}$. In the CMS, M_{bc} can be expressed as follows:

$$M_{bc} = \sqrt{\frac{s}{4} - (\vec{p}_{\ell\gamma})^2} \quad (3.6)$$

The signal region is the ellipse selecting events around the expected values $M_{bc} \simeq m_\tau$ and $\Delta E/\sqrt{s} \simeq 0$. Figure 3.8 shows the distributions of $\Delta E/\sqrt{s}$ and M_{bc} for the $\tau \rightarrow \mu\gamma$ and $\tau \rightarrow e\gamma$ search.

In the 2σ signal region, the overall signal efficiency estimated is 2.9% for

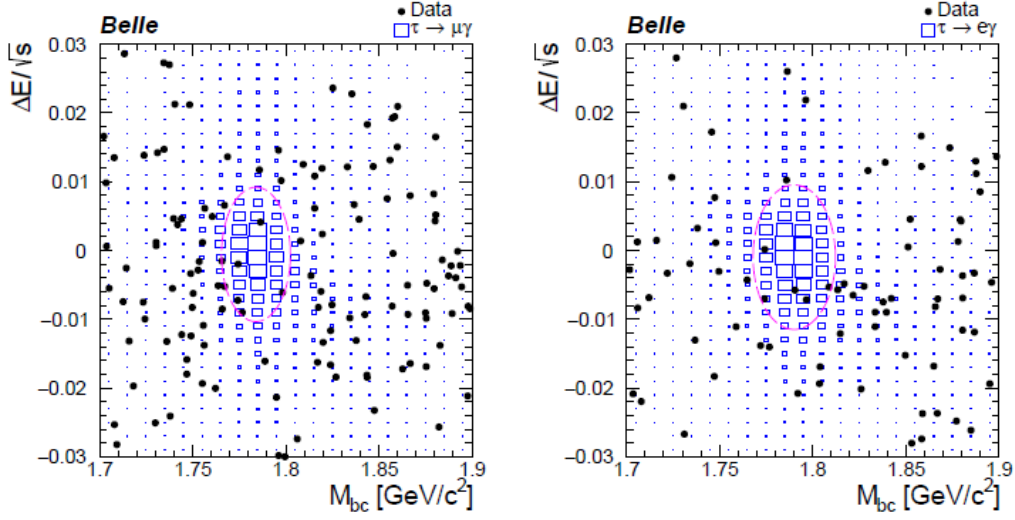


Figure 3.8: Two dimensional distributions for $\tau \rightarrow \mu\gamma$ (left) and $\tau \rightarrow e\gamma$ (right) events. Black points are data, blue squares are $\tau^\pm \rightarrow \ell^\pm\gamma$ signal MC events and magenta ellipses show the 2σ signal region used in the Belle analysis.

$\tau^\pm \rightarrow e^\pm\gamma$ and 3.7% for $\tau^\pm \rightarrow \mu^\pm\gamma$.

The estimated systematic uncertainties account for 3.3% for $\tau^\pm \rightarrow \mu^\pm\gamma$ and 3.7% for $\tau^\pm \rightarrow e^\pm\gamma$. These values are associated with track and photon reconstruction efficiencies, photon energy calibration, luminosity, trigger efficiencies and background PDF modeling. The observed upper limits, at the 90% C.L., on the branching fractions are thus $\mathcal{B}(\tau^\pm \rightarrow \mu^\pm\gamma) < 4.2 \times 10^{-8}$ and $\mathcal{B}(\tau^\pm \rightarrow e^\pm\gamma) < 5.6 \times 10^{-8}$.

4

Analysis Overview

As already said, the BaBar and Belle experiments set the most stringent upper limits to date on the measurements, respectively, of the $\tau \rightarrow e\gamma$ and $\tau \rightarrow \mu\gamma$ decays.

Using the data collected so far with the Belle II detector, that correspond to an integrated luminosity of 424 fb^{-1} , it may be to improve these measurements. This dataset is clearly smaller respect to that available both at Belle and at BaBar. Thus, to reach competitive results, it is necessary to improve the statistical power of the dataset, including additional channels for the selection of the event. The BaBar analysis, in fact, reached competitive results with Belle in terms of the $\tau \rightarrow e\gamma$ search, even with a smaller dataset available. BaBar searched for $\tau \rightarrow \ell\gamma$ decays by reconstructing events displaying a 1x1 or 3x1 topology, while the Belle experiment based its search on a 1x1 topology only.

For the Belle II analysis, we plan to use both tagging topologies to improve the statistical power of the analysis, at a given luminosity. In this thesis, I developed the selection criteria for a $\tau \rightarrow \ell\gamma$ decay in the case of events displaying a 3x1 topology, which is used for the first time in Belle II. The selection has been developed with a target luminosity of 500 fb^{-1} , corresponding to the data data would have been expected at Belle II before the first technical Long Shutdown in 2022.

4.1 DATASET

This analysis uses Monte Carlo (MC) simulated samples to optimize the event selection as well as to estimate signal and background contributions. Several Standard Model e^+e^- final states contribute to the analysis as background: $q\bar{q}$ where $q = u, d, c, s, b$ (hadronic), $\ell^+\ell^-\gamma$ (dileptonic), $e^+e^-\ell^+\ell^-$ (four-fermionic) events.

To simulate the production of the $\tau^+\tau^-$, $q\bar{q}$ (with $q = u, d, c, s$) and $\mu^+\mu^-(\gamma)$ samples the KKMC generator is employed [41][42]; BabaYaga@NLO simulates the Bhabha scattering $e^+e^- \rightarrow e^+e^-(\gamma)$ [43][44][45][46][47]; $B\bar{B}$ events are generated with EvtGen, while non radiative four-fermionic events are generated with AAFH and TREPS [48][49][50][51]. Standard Model τ decays are handled by TAUOLA [52] and their radiative corrections by PHOTOS [53].

The Belle II Analysis Software Framework (*basf2*) [29], *release-05-02-00*, uses the Geant4 package for the simulation of the response of the detector [54].

4.1.1 BACKGROUND PROCESSES

For the studies of event selection and background suppression, the most recent available version of Monte Carlo has been used, the official Early Phase 3 MC14 campaign. A summary table of the reconstructed background processes is reported in Table 4.1.

Process	$\int \mathcal{L} dt$ [ab^{-1}]	Cross section [nb]	Background label
$e^+e^- \rightarrow \tau^+\tau^-$	1	0.919	'taupair'
$e^+e^- \rightarrow u\bar{u}$	1	1.605	
$e^+e^- \rightarrow d\bar{d}$	1	0.401	
$e^+e^- \rightarrow c\bar{c}$	1	1.329	'hadron'
$e^+e^- \rightarrow s\bar{s}$	1	0.383	
$e^+e^- \rightarrow e^+e^-(\gamma)$	0.1	295.8	'ee'
$e^+e^- \rightarrow \mu^+\mu^-(\gamma)$	1	1.148	'mumu'
$e^+e^- \rightarrow e^+e^-e^+e^-$	0.2	39.55	
$e^+e^- \rightarrow e^+e^-\mu^+\mu^-$	0.2	18.83	'low multiplicity'

Table 4.1: MC14 background samples with their total generated luminosity.

Other MC samples, like $e^+e^- \rightarrow \mu^+\mu^-\mu^+\mu^-$, $e^+e^-\tau^+\tau^-$, $\mu^+\mu^-\tau^+\tau^-$, $\tau^+\tau^-\tau^+\tau^-$,

$e^+e^-\pi^+\pi^-$, $e^+e^-K^+K^-$, $\pi^+\pi^-(\pi^0)$, K^+K^- , $K^0\bar{K}^0$ were generated and reconstructed, but did not survive the reconstruction cuts and will be therefore omitted in the present analysis.

4.1.2 SIGNAL EVENTS

Signal MC samples are $\tau^+\tau^-$ events, with one of the τ 's decaying to $\ell\gamma$ and the other generically, according to the SM branching fractions. An amount of $2 \cdot 10^6$ signal events are generated for both the $\tau^+ \rightarrow e^+\gamma$ and the $\tau^+ \rightarrow \mu^+\gamma$ search. An equal number of events are generated for the charge conjugated LFV τ decays.

4.2 EVENT RECONSTRUCTION AND PRE-SELECTIONS

In the $e^+e^- \rightarrow \tau^+\tau^-$ centre-of-mass system (CMS), the τ leptons decay products are well separated in two opposite hemispheres, approximately, by the plane perpendicular to the thrust axis \hat{n}_{thrust} , as already defined in (3.1). One hemisphere is expected to contain the products of the 3-prong decay, while the other one should contain the signal $\tau \rightarrow \ell\gamma$ (here, the photon is constrained to come to the same primary vertex as the lepton.).

Similarly, the photons and the π^0 s are separated into hemispheres.

Figure 4.1 illustrates the 3x1 topology, in the centre of momentum system (CMS). The signal-side is expected to contain the τ decays to a muon or an electron and a photon, for the $\tau^\pm \rightarrow \mu^\pm\gamma$ or $\tau^\pm \rightarrow e^\pm\gamma$ search, while in the tag-side the τ undergoes decays according the SM processes $\tau \rightarrow 3\pi(\pi^0)\nu$.

4.2.1 RECONSTRUCTION CRITERIA

Due to the short lifetime of the τ lepton, its decay products are expected to originate near the interaction point. The signal candidates are selected by requiring the following constraints on charged tracks and neutral particles.

CHARGED TRACKS

Tracks must satisfy the following conditions:

4.2. EVENT RECONSTRUCTION AND PRE-SELECTIONS

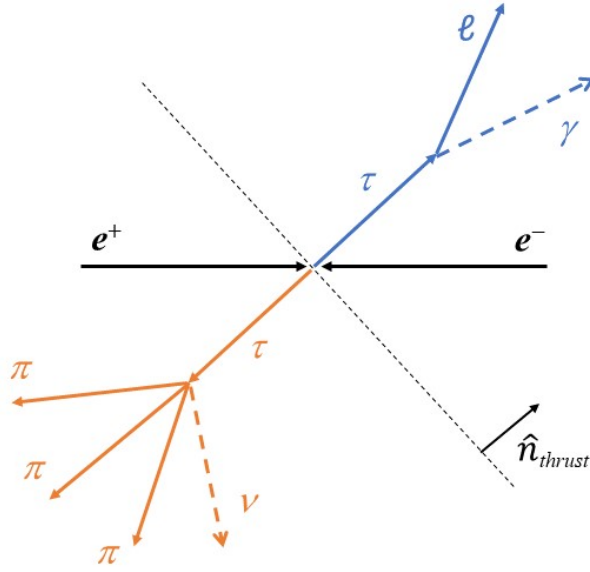


Figure 4.1: The 3x1 topology in the centre of momentum system (CMS) for a typical signal event.

- exactly four charged tracks are required, coming from the interaction point: the event is separated into two hemispheres, only one track is expected in the signal-side and three in the tag-side;
- $Q_{TOT} = 0$, i.e. zero net charge;
- $|dz| < 3$ cm;
- $dr < 1$ cm.

Charged particle tracks can be identified in the detector by a combination of discriminants, such as dE/dx as measured by the CDC and shower shape in the ECL. Probability density functions (PDFs) for these discriminants are well known quantities for many elementary particles. Likelihood probabilities can be calculated combining each PDF to produce a final likelihood variable. This is known as the *likelihood ratio* \mathcal{L} , with range from 0 to 1. Particle identification at Belle II uses particle identification (PID) values for candidate tracks.

On one-prong tracks a constraint on particle identification is required for both the searches: $\mathcal{L}_e > 0.9$ for $\tau \rightarrow e\gamma$ and $\mathcal{L}_\mu > 0.9$ $\tau \rightarrow \mu\gamma$.

On three-prong tracks no particle identification is needed. In fact, it's very unlikely a contamination of a three prong tag from a radiative three-prong $\tau \rightarrow \ell\nu\bar{\nu}\gamma(\rightarrow \ell\ell)$ process.

NEUTRAL PARTICLES

Neutral particles, precisely photons and π^0 , are involved in the reconstruction of a candidate event. Among the three-prong tag decay modes, the channel $\tau^\pm \rightarrow \pi^\pm \pi^+ \pi^- \pi^0 \nu_\tau^{(\pm)}$ is also included to increase the statistics, allowing the presence of π^0 's in the tag-side. As regards the number of neutral pions in the signal-side, we reject completely the presence of π^0 's to suppress $\tau \rightarrow \pi \pi^0 (\rightarrow 2\gamma) \nu$ and $q\bar{q}$ backgrounds events.

Neutral pions are kept in the analysis through their decays $\pi^0 \rightarrow \gamma\gamma$. Photons that are used to reconstruct π^0 's are required to satisfy the following conditions:

- $\text{clusterNHits} > 1.5$ (number of weighted crystals in the ECLCluster),
- $-0.8660 < \cos\theta < 0.9565$ (in the CDC acceptance),
- $|\text{cluster timing}| < 200 \text{ ns}$,
- $0.115 \text{ GeV}/c^2 < M_{\gamma\gamma} < 0.152 \text{ GeV}/c^2$.

The photons which are not used in the π^0 reconstruction and pass the following energy threshold

- $E_\gamma > 0.2 \text{ GeV}$

are kept in the analysis and used for the reconstruction of the signal-side τ .

To summarize on the presence of neutral particles in the reconstructed event, we allow for:

- $N_{\pi^0}^{\text{sig-side}} = 0, \quad N_{\pi^0}^{\text{tag-side}} \leq 1,$
- $N_\gamma^{\text{sig-side}} = 1.$

In the following of this text we will refer to these requirements on neutral particles also as *neutral vetoes*.

4.2.2 PRE-SELECTIONS

P_T ORDERING OF TRACKS ON THE 3-PRONG SIDE

The 3-prong tag sample can be contaminated by a 1-prong tau decay reconstructed with the addition of slow e^+e^- pair coming from background photon conversion. To remove this contamination, a specific selection on the transverse momentum of the three tracks of the tag-side has been studied.

4.3. EVENT SELECTION AND BACKGROUND SUPPRESSION

We optimized using the *taupair* sample to suppress all the other SM backgrounds, since the tag side of the taupair sample is the same of the $\tau \rightarrow \ell\gamma$ sample. The optimization is performed using the figure of merit (FOM)

$$\frac{S}{\sqrt{S+B}} \quad (4.1)$$

where S and B are the number, respectively, of taupair and background events after the selection.

The tracks are sorted from the highest to lowest transverse momentum and referred as "leading", "subleading" and "third". The result of the optimization for the three tracks is reported in Table 4.2, both for the muon and electron channel. The much stronger cuts on the electron channel reflect the need to suppress the much higher $ee \rightarrow ee(\gamma)$ background.

P_T ordering [GeV/c]	muon channel	electron channel
leading	$P_T > 0.14$	$P_T > 0.49$
subleading	$P_T > 0.14$	$P_T > 0.38$
third	$P_T > 0.06$	$P_T > 0.15$

Table 4.2: Optimized selection for the tag-side transverse momenta.

Figure 4.2 displays the distributions of the transverse momentum for the three tracks and the cuts obtained from the optimization process.

1-PRONG SIDE PRE-SELECTION

Another further pre-selection on 1-prong side particles is applied to the kinematic variables:

- $1 \text{ GeV}/c^2 < M_{inv,\ell\gamma} < 2 \text{ GeV}/c^2$,
- $-1.5 \text{ GeV} < \Delta E < 0.5 \text{ GeV}$,

to select a narrow window, containing signal events and rejecting background.

4.3 EVENT SELECTION AND BACKGROUND SUPPRESSION

In this analysis we are interested in the sensitivity of the search for a rare phenomena, namely $\tau \rightarrow \ell\gamma$.

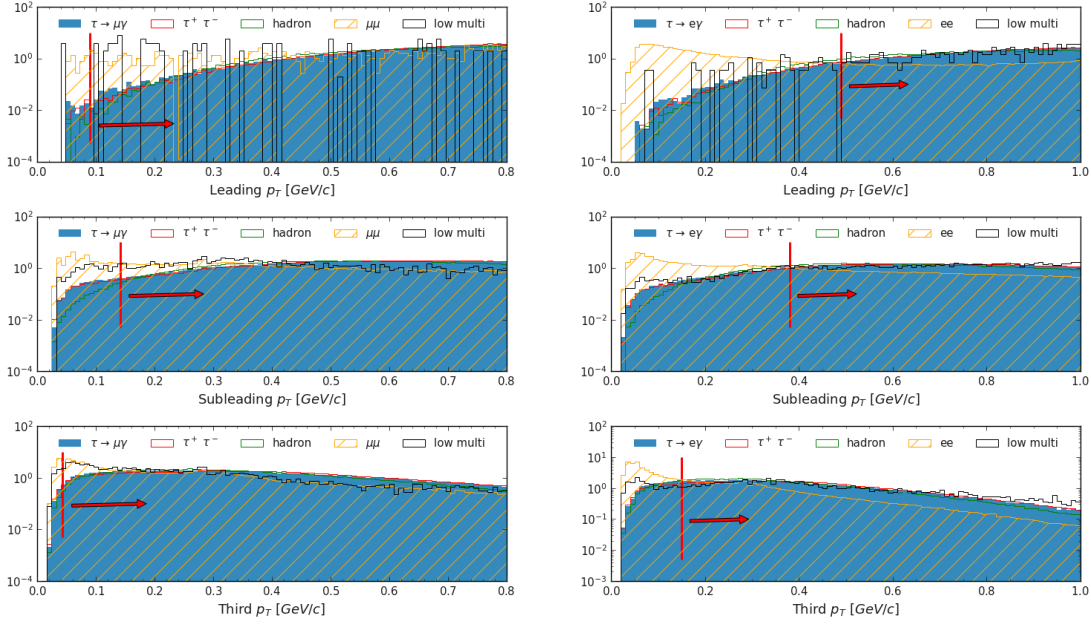


Figure 4.2: Transverse momentum distributions for the three tracks in the tag-side. Plots for the muon channel are on the left side of the figure, those for the electron one are on the right. Red lines indicate the optimized cuts of Table 4.2, the arrows point to the fractions of events selected by the cuts.

4.3.1 FIGURE OF MERIT

In order to maximize our sensitivity to the $\tau \rightarrow \ell\gamma$ decay we developed a selection based on variables with strong signal/background discrimination power. All the selection criteria are optimized in order to maximize the search sensitivity at the 90% confidence level (CL). The set of cuts that are optimal for the event selection and background suppression is determined by maximizing the *Punzi Figure Of Merit* [55]

$$\frac{\epsilon(t)}{\frac{a}{2} + \sqrt{B(t)}} \quad (4.2)$$

since it is independent of a-priori expectations about the unknown $\tau \rightarrow \ell\gamma$ decay.

Here,

- $\epsilon(t)$ is the signal efficiency for the chosen cuts t ,
- $B(t)$ is the number of background events at a given luminosity,
- $a = 1.28$ is the number of sigmas for a one-sided Gaussian test at our chosen significance.

4.3. EVENT SELECTION AND BACKGROUND SUPPRESSION

The MC14 campaign simulates typical e^+e^- collisions at an integrated luminosity of 1 ab^{-1} . As above mentioned, our target luminosity is 500 fb^{-1} , thus, in our analysis the number of background events will be properly rescaled by a factor $\frac{1}{2}$.

4.3.2 SELECTION VARIABLES

The selection involves the following variables:

- $\cos\theta_{\ell\gamma,CMS}$: the cosine of the angle between the lepton and photon in the CMS,
- $E_{visible}^{CMS}$: the visible energy of the event in the CMS. Here, $E_{visible}^{CMS} = \sum_i E_i^{CMS}$ is the sum of the energies E_i^{CMS} of all tracks and photons in the final state,
- M_{miss}^2 : the missing mass of the event. In the CMS, the variable can be defined as follows $M_{miss}^2 = (E_{beam} - E_{visible}^{CMS})^2 - |\vec{P}_{vis}^{CMS}|^2$
- *Thrust* value, as defined in (3.1).

It is worth to note that the research of the optimal cut for the variables does not always involve all the SM background samples, but, in some cases, only some of them. For example, for the $\cos\theta_{\ell\gamma,CMS}$ and *Thrust* variables, it is not possible to suppress some specific background and the maximization of the Punzi FOM will be performed with the aim to suppress all the SM processes. On the other hand, the M_{miss}^2 variable can be useful to suppress the *taupair* sample, while the $E_{visible}^{CMS}$ the *low multiplicity, hadron* and *mumu* samples. These arguments become clear looking at Figure 4.3, where the distributions of all the aforementioned variables are displayed. Plots are referred to the muon case. Those regarding the electron one are totally similar. These plots are meant to be interpreted as the events left after the pre-selections 4.2.2 are applied.

4.3.3 SIMULATED ANNEALING

The process of the optimization of the selection lies in the search for a global maximum of a given function, the Punzi Figure Of Merit in our case. Originally, the selection has been optimized in a sequential manner, meaning that an optimal cut was found one variable after the other. This method presents an immediate issue, since the selection varies critically according to the order chosen for the variables in the cutflow: different orderings give different selections.

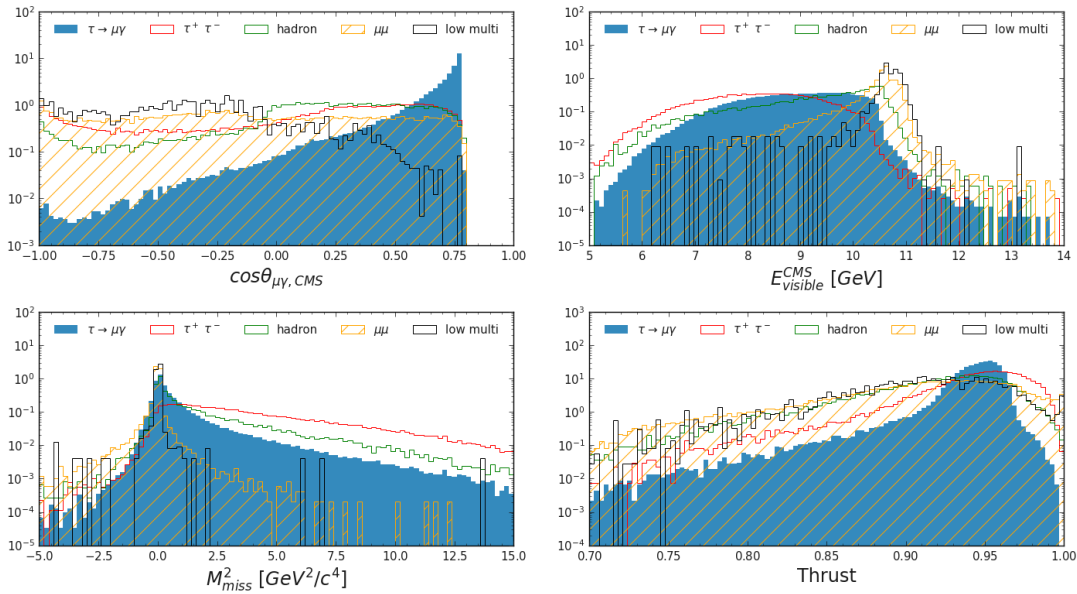


Figure 4.3: Distributions of the variables involved in the optimization of the selection for the muon channel.

To avoid similar problems, a different approach can be adopted by using algorithms that act simultaneously on all the variables. In our analysis, the tool used for the optimization of the selection is the Simulated Annealing.

The Simulated Annealing (SA) is an algorithm [56] to approximate the global optimum of an objective function in a large search space. Its operations depend on a parameter, the *temperature* T , that controls the randomized search. The SA generates a sequence of random samples \mathbf{x} , the set of the selection cuts in our case, and then move around the search space, proposing, at every iteration, a candidate transition from \mathbf{x} to \mathbf{x}' . The transition $\mathbf{x} \rightarrow \mathbf{x}'$ is accepted with probability

$$\begin{cases} 1 & \text{if } \Delta y \leq 0 \\ e^{-\Delta y/T} & \text{if } \Delta y > 0 \end{cases}$$

where $\Delta y = f(\mathbf{x}') - f(\mathbf{x})$ is the difference in the objective function $f(\mathbf{x})$ and T is the temperature parameter.

The probability function allows to accept worse solutions ($\Delta y > 0$) at the beginning of the search, when the temperature is high, and to suppress them with the progress of the search, when the temperature decreases. The role of the temperature parameter is to give the algorithm the opportunity, when T is high, to freely move about the search space, escaping also local optima, and, when T

4.4. OPTIMIZATION OF THE SELECTION

is slowly reduced, to locate the region for the global optima. The search is then forced to converge to a minimum.

4.4 OPTIMIZATION OF THE SELECTION

The $\tau \rightarrow \ell\gamma$ decay will be searched in a region that is elliptical in the kinematic variables $M_{inv,\ell\gamma}$ and ΔE (see Figure 3.4) and contains around the 95% of the signal.

The optimization of the selection needs to be performed nearby the signal region, where signal events are more likely to be found. However, the signal region can be defined only after a selection has been developed. To be sure that the Simulated Annealing does not suppress background too far from this region, we defined an optimization region that approximates the signal one in number of signal events contained. A preliminary selection will be optimized inside the optimization region and will be then used to define a more realistic region where we will perform the analysis.

4.4.1 OPTIMIZATION REGION

The region defined for the optimization is two-dimensional in the variables M_{BC} and ΔE .

ΔE has been already defined in eq (3.3). M_{BC} is the *beam-constrained mass* already defined in (3.6). It can be easily proved that, thanks to the energy conservation law

$$|\vec{p}_\gamma| = E_\gamma = \frac{\sqrt{s}}{2} - E_\ell, \quad (4.3)$$

the dependence of M_{BC} on \vec{p}_γ can be factored out

$$M_{BC} = \sqrt{\frac{s}{4} - (\vec{p}_{\ell\gamma})^2} \quad (4.4)$$

$$= \sqrt{\frac{s}{4} - (\vec{p}_\ell + \vec{p}_\gamma)^2} \quad (4.5)$$

$$= \sqrt{\frac{s}{4} - \left(|\vec{p}_\ell|^2 + |\vec{p}_\gamma|^2 + 2|\vec{p}_\ell||\vec{p}_\gamma|\cos\theta_{\ell\gamma} \right)}. \quad (4.6)$$

showing how M_{BC} only depends on \sqrt{s} , \vec{p}_ℓ , E_ℓ and $\theta_{\ell\gamma}$. The M_{BC} variable

provides a better resolution for the reconstructed mass with respect to the $M_{inv,\ell\gamma}$ of (3.2) by avoiding a dependence on the E_γ resolution.

The optimization region is defined through rectangular cuts at the 1st and 99th percentile, so as to include the 98% of the signal for both the variables. The overall coverage of this two-dimensional region is approximately 96%. The set of cuts that define such optimization region is reported in Table 4.3.

	M_{BC} [GeV/c^2]	ΔE [GeV]
<i>muon channel</i>	$1.70 < M_{BC} < 3.04$	$-1.31 < \Delta E < 0.09$
<i>electron channel</i>	$1.66 < M_{BC} < 2.97$	$-1.31 < \Delta E < 0.09$

Table 4.3: Cuts on the M_{BC} and ΔE variables that define the optimization region.

Figure 4.4 displays the distributions of the variables M_{BC} and ΔE . Red lines represent the cuts of Table 4.3 that delimit the optimization region.

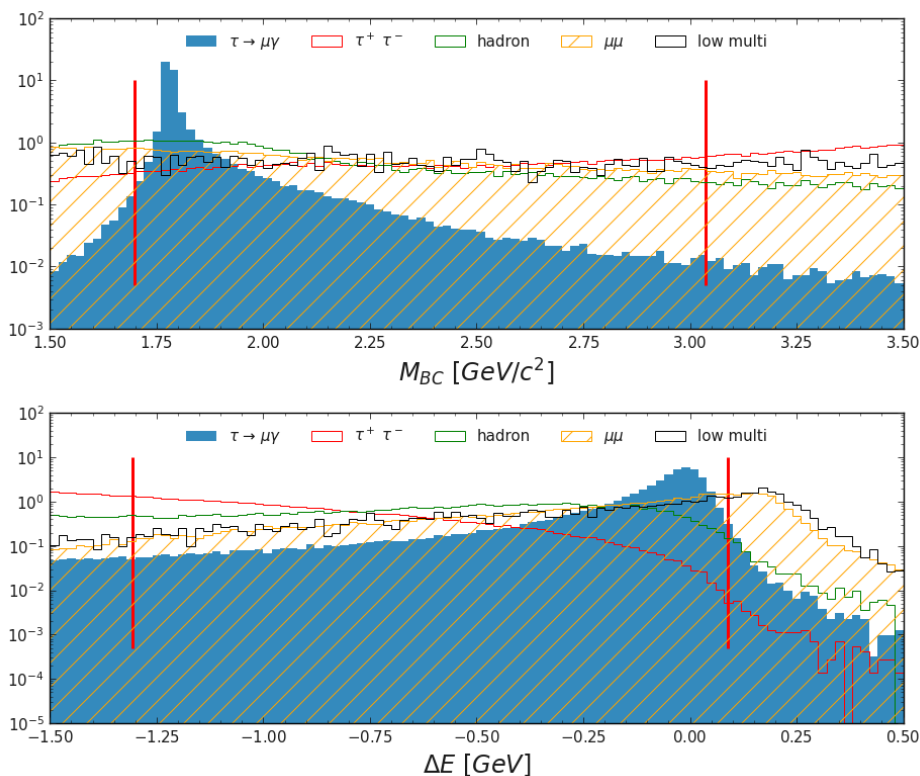


Figure 4.4: Distributions of the variables M_{BC} and ΔE for the muon case. Red lines represent the cuts that delimit the optimization region.

A preliminary optimization of the selection is thus performed into this region (to which we will refer also as “box region”).

4.4. OPTIMIZATION OF THE SELECTION

OPTIMIZATION IN THE BOX REGION

Of the four variables involved for the development of the selection, our strategy will be to use a hand cut for $\cos\theta_{\ell\gamma,CMS}$ and to optimize the selection for the remaining three variables with the Simulated Annealing. This choice is motivated by the strong correlation between the $\theta_{\ell\gamma}$ and M_{BC} variables. As already known in literature [35], a reasonable cut that can provide an optimal signal selection is $0.4 < \cos\theta_{\ell\gamma,CMS} < 0.8$. This cut is imposed both for the muon and the electron case, as shown in Figure 4.5.

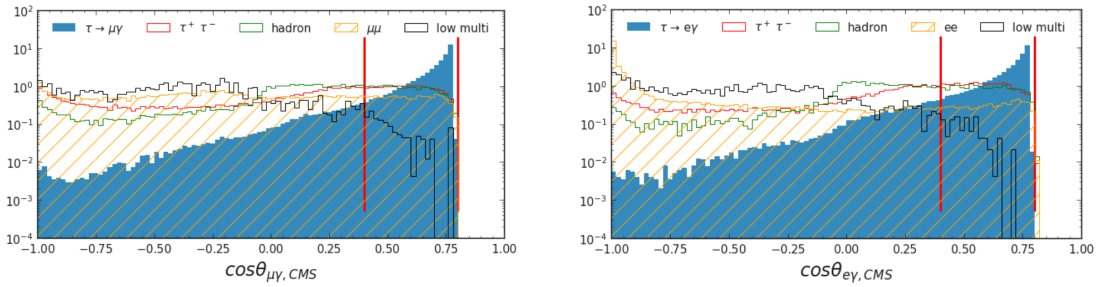


Figure 4.5: Distribution of $\cos\theta_{\mu\gamma,CMS}$ (on the left) and $\cos\theta_{e\gamma,CMS}$ (on the right). Red lines indicate the adopted cut.

The other three variables, $E_{visible}^{CMS}$, M_{miss}^2 and $Thrust$, are thus optimized with the Simulated Annealing. Inside the box region, the SA provided the set of cuts reported in Table 4.4.

	$\tau \rightarrow \mu\gamma$ search	$\tau \rightarrow e\gamma$ search
Punzi FOM	1624	744
Visible energy [GeV]	$E_{visible}^{CMS} < 10.3$	$E_{visible}^{CMS} < 10.3$
Missing Mass [GeV^2/c^4]	$M_{miss}^2 < 1.20$	$M_{miss}^2 < 2.55$
Thrust value	$0.93 < Thrust < 0.96$	$0.93 < Thrust < 0.96$

Table 4.4: Selection provided by the Simulated Annealing for the optimization into the box region.

The variables distributions, with the corresponding optimal cuts, are shown in Figure 4.6. The arrows point to the events surviving the cuts.

We can now evaluate the effect of our selections on the simulated data. In particular, we are interested in knowing the value of the signal selection efficiency $\epsilon(t)$ and the number of background events left into the box region.

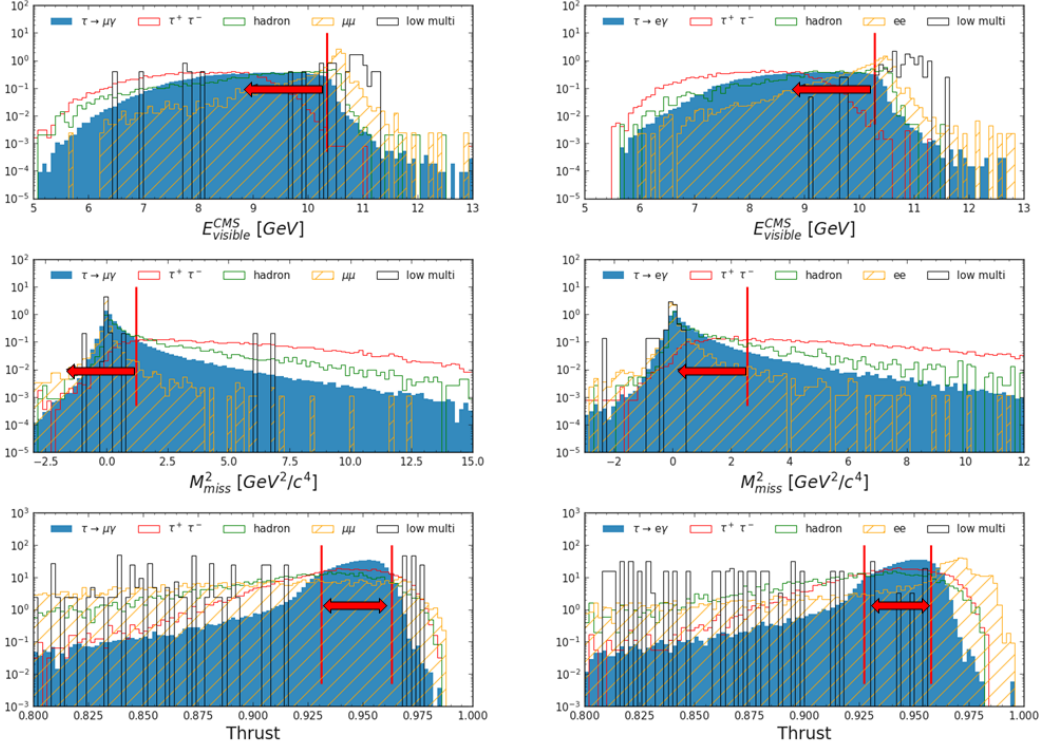


Figure 4.6: Variables distributions and the set of cuts of Table 4.4. Arrows point to the events surviving after the optimization.

When applying the pre-selections, the constraint on $\cos\theta_{\ell\gamma}$ and the cuts of Table 4.4, the result of the selection on data is that reported in Table 4.5, for the muon case, and 4.6, for the electron case.

Table 4.5: Result of the first selection for the muon case.

$\epsilon(t)$	Background Events
2.4%	taupair 502
	hadron 585
	low multiplicity 0
	mumu 215

Table 4.6: Result of the first selection for the electron case.

$\epsilon(t)$	Background Events
1.5%	taupair 662
	hadron 320
	low multiplicity 3
	ee 2030

We can decide also to apply the selection without the requirement of neutral particles, i.e. removing the constraint on the number of γ 's and π^0 's at the reconstruction level. From this choice we can expect an increase in the number of events, both of signal and background, since we are removing some restrictions on data. Tables 4.7 and 4.8 report, the signal efficiency and the number of

4.4. OPTIMIZATION OF THE SELECTION

background events when the neutral vetoes are removed from the selections.

Table 4.7: Result of the first selection for the muon case.

$\epsilon(t)$	Background Events
4.0%	taupair 1471
	hadron 2711
	low multiplicity 0
	mumu 261

Table 4.8: Result of the first selection for the electron case.

$\epsilon(t)$	Background Events
2.6%	taupair 1942
	hadron 2374
	low multiplicity 3
	ee 3845

As expected, more signal and background events are left in the box region when relaxing neutral vetoes. However, the high number of background events remained shows that more stringent selections must be still developed.

4.4.2 SIGNAL REGION

The selection developed in the box region allows to define the signal region into which the final selection will be optimized.

The signal region is elliptical in M_{BC} and ΔE , centered around the mode of the signal for these two variables. The ellipse is chosen so as to contain about 95% of the signal left from our previous selections. Such signal region is displayed in Figure 4.7, on the left, for the muon case and, on the right, for the electron case.

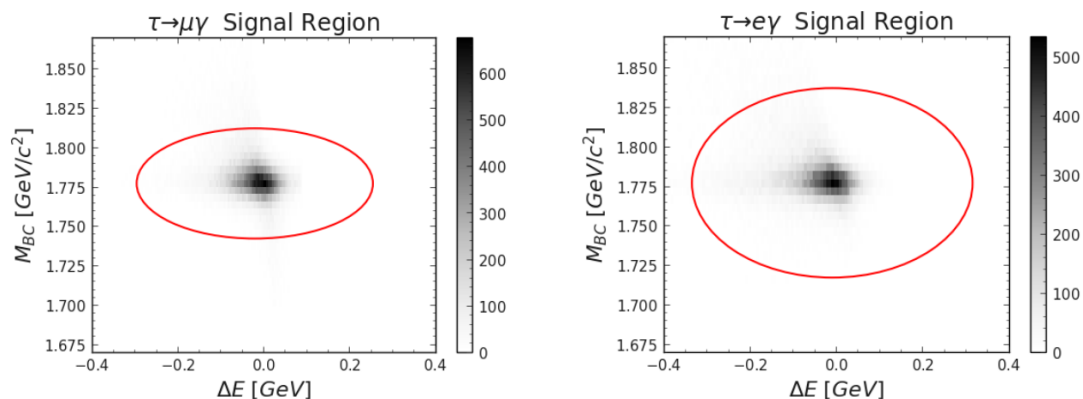


Figure 4.7: Signal region for the $\tau \rightarrow \mu\gamma$ search, on the left, and for the $\tau \rightarrow e\gamma$ search, on the right.

We can see from the above figure that, respect to the $\tau \rightarrow \mu\gamma$ search, a bigger signal region is defined for the $\tau \rightarrow e\gamma$ search. This will have effect also on the

upcoming optimization and on final results, since more background is being included into the electronic signal region.

OPTIMIZATION IN THE SIGNAL REGION

A new optimization of the selection is now performed into the elliptical region above described. In the same way as before, we use a hand cut for $\cos\theta_{\ell\gamma}$ and optimize the other variables with the Simulated Annealing.

The selection in Table 4.4 allows also to find a new and more stringent cut for $\cos\theta_{\ell\gamma}$. Figure 4.8 shows the distribution of the events left after the first selection. The chosen cut is now $0.67 < \cos\theta_{\ell\gamma} < 0.78$ for both the muon and electron cases.

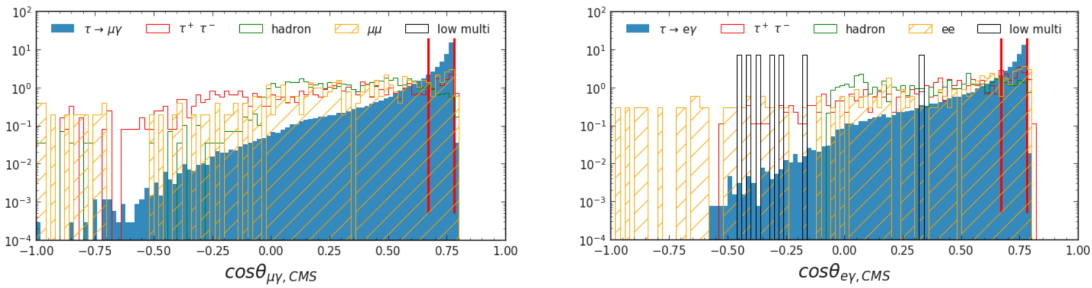


Figure 4.8: $\cos\theta_{\mu\gamma,CMS}$ (on the left) and $\cos\theta_{e\gamma,CMS}$ (on the right) distributions for the events left after the first optimization.

The selection for the other variables is thus optimized into the signal region. The Simulated Annealing provided, for both the searches, the set of cuts reported in Table 4.9. In the same table a comparison with the previous selection is also presented.

We can see from Table 4.9 that, while for the muon case the selections optimized into different regions are almost the same, those for the electron case share some differences. In particular, the cuts relative to the variables $E_{visible}^{CMS}$ and M_{miss}^2 are more relaxed in the second optimization, meaning that more background can be expected in the $\tau \rightarrow e\gamma$ search.

However, it should also be noted that in the second optimization we have an increase, for both the searches, in the value of the Punzi Figure Of Merit, meaning that a stronger background suppression is achieved into the signal region by the new selection.

Figure 4.9 shows the number of background events left into the signal region from the second selection. We can see from the figure the strong background

4.4. OPTIMIZATION OF THE SELECTION

$\tau \rightarrow \mu\gamma$ search		
	1 st Selection	2 nd Selection
Punzi FOM	1624	6384
Visible energy [GeV]	$E_{visible}^{CMS} < 10.3$	$E_{visible}^{CMS} < 9.93$
Missing Mass [GeV^2/c^4]	$M_{miss}^2 < 1.2$	$M_{miss}^2 < 0.90$
Thrust value	$0.93 < Thrust < 0.96$	$0.92 < Thrust < 0.96$
$\tau \rightarrow e\gamma$ search		
	1 st Selection	2 nd Selection
Punzi FOM	744	1137
Visible energy [GeV]	$E_{visible}^{CMS} < 10.3$	$E_{visible}^{CMS} < 11.9$
Missing Mass [GeV^2/c^4]	$M_{miss}^2 < 2.4$	$M_{miss}^2 < 4.45$
Thrust value	$0.93 < Thrust < 0.96$	$0.93 < Thrust < 0.96$

Table 4.9: Comparison between the first selection (optimized into the box region) and the second selection (optimized into the signal region) developed for the $\tau \rightarrow \mu\gamma$ and $\tau \rightarrow e\gamma$ searches.

suppression achieved by the selection for the $\tau \rightarrow \mu\gamma$ search. As regards the $\tau \rightarrow e\gamma$ search, more background remains into the signal region, both because of the size of the region itself and also because of the more relaxed selections. The effective number of background events left into the signal region is reported in the Tables 4.10 and 4.11. At this point it should be remembered that the MC14 campaign simulates data at a luminosity of 1 ab^{-1} . Since our analysis is performed with a target luminosity of 0.5 ab^{-1} , all the background events in the present table have been rescaled by a factor $1/2$.

Both the tables contain also the the signal efficiency in the case of neutral vetoes applied to the data.

$\epsilon(t)$	Background events
1.4%	taupair 3
	hadron 2.5
	low multiplicity 0
	mumu 1

Table 4.10: Result of the second selection for the muon case.

$\epsilon(t)$	Background events
1.2%	taupair 6
	hadron 15.5
	low multiplicity 0
	ee 21.5

Table 4.11: Result of the second selection for the electron case.

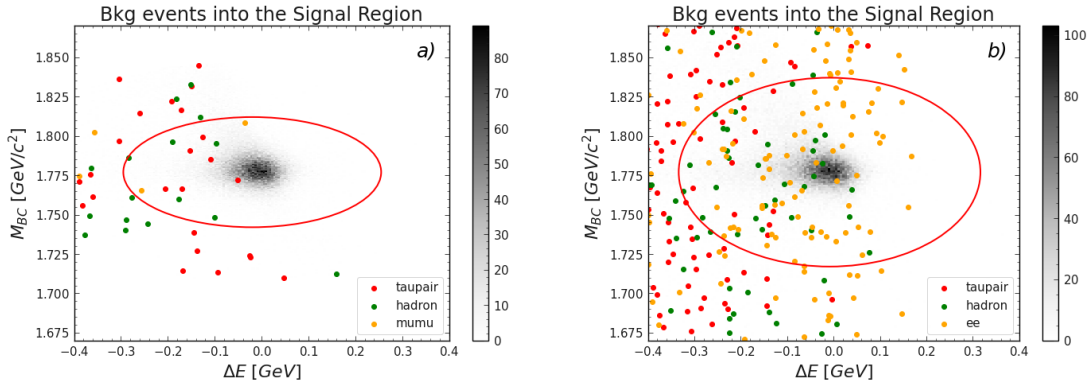


Figure 4.9: Background events left into the signal region from the second selection. Plot *a)* is for the $\tau \rightarrow \mu\gamma$ search, plot *b)* for the $\tau \rightarrow e\gamma$ search. Neutral vetoes are applied to data.

We could now decide to apply the selection to our data without the requirements on neutral particles. We remember that this implies admitting into the global event the presence of additional photons and of π^0 's.

As regards the $\tau \rightarrow e\gamma$ decay, this choice might be troublesome, since the electron is particularly subject to bremsstrahlung radiation. Having more photons in the global event means that, at the moment of the reconstruction of the event, we deal with multiple photon candidates that can be associated to the $\tau \rightarrow \ell\gamma$ decay. Thus, additional photons can be allowed only if we are sure about their origin, if they have been radiated or if they actually come from a τ decay. This could be achieved by a proper photon energy correction, but a specific study must be conducted on this topic and it is not ready at this stage. For what concerns the presence of π^0 's, we decided to still maintain this veto since it preserves the analysis from $q\bar{q}$ background. Thus, all the vetoes on neutral particles will be kept for the electron case during the whole analysis.

Instead, as regards the muon, it is known that bremsstrahlung phenomena are much less likely to occur. Relaxing the veto on the number of photons is something less problematic in this case. However, we still maintain the veto on the number of π^0 's. Figure 4.10 shows the background events left into the signal region when additional photons are allowed in the $\tau \rightarrow \mu\gamma$ search.

We are left with a slightly higher number of background events when additional photons are admitted in $\tau \rightarrow \mu\gamma$ search. The increase in the background events and the new signal efficiency are reported in Table 4.12. These are the quantities that we will use for our sensitivity estimate of the $\tau \rightarrow \mu\gamma$ decay.

4.4. OPTIMIZATION OF THE SELECTION

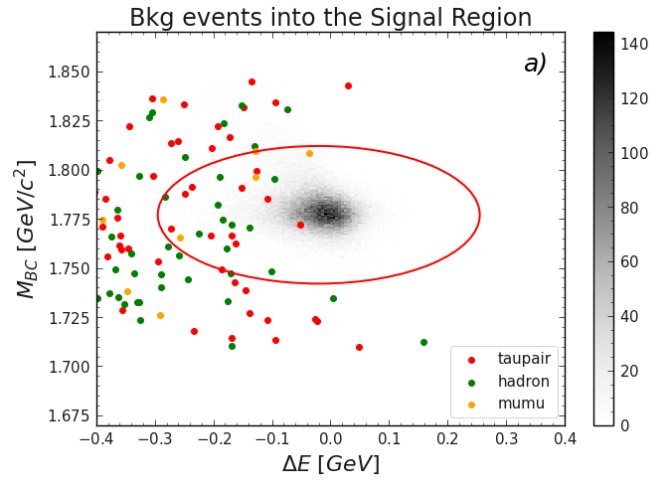


Figure 4.10: Background events left into the signal region from the second selection for the $\tau \rightarrow \mu\gamma$ search. Additional photons are admitted in this plot.

$\epsilon(t)$	Background events
2.4%	taupair 4
	hadron 5
	low multiplicity 0
	mumu 1.5

Table 4.12: Result of the second selection for the muon case when additional photons are admitted in the global event.

5

Results and Conclusions

A sensitivity estimate to the measurement of the $\tau \rightarrow \ell\gamma$ decay is given in the present chapter to contextualise the results of the optimisation. We provide results both for our studied case of a 3x1 topology as well as the case of a 1x1 topology taken from the study performed by another group in the Belle II collaboration. We then estimate the 90% C.L. upper limit to the $\mathcal{B}(\tau \rightarrow \ell\gamma)$ by combining the results from the two selections.

Finally, since the present analysis is preliminary to quantify the impact on the sensitivity when more inclusive approaches for the $\tau \rightarrow \ell\gamma$ decay are adopted, we comment on typical systematic effects and possible future improvements.

5.1 SENSITIVITY ESTIMATE

Given the results obtained in the previous chapter, we want now to give an estimate of the sensitivity to the $\tau \rightarrow \ell\gamma$ decay for our measurement, i.e., the average upper limit that would be obtained by an ensemble of experiments in the hypothesis of a certain expected background and no true signal. For the case of a measurement of a Poisson variable, the Feldman-Cousins method provides a value for the experimental sensitivity at a desired confidence level [57]. In our case, we want to set an 90% C.L. upper limit to the branching fraction of the $\tau \rightarrow \ell\gamma$ decay in the hypothesis of no signal.

5.1.1 RESULTS OF THE 3x1 AND 1x1 TOPOLOGIES

The results of the previous chapter reported the expected number of background events in the signal region and the signal efficiency, as estimated from the simulated data. Table 5.1 reports a summary of these results and the upper limit on N_{sign} established with the Feldman-Cousins method.

	$\tau \rightarrow \mu\gamma$			$\tau \rightarrow e\gamma$		
	N_{bkg}	UL(N_{sign})	$\epsilon(t)$	N_{bkg}	UL(N_{sign})	$\epsilon(t)$
Without additional γ 's	6.5	5.7	1.4%	43	12.03	1.2%
With additional γ 's	11.5	7.1	2.4%	-	-	-

Table 5.1: Number of background events and upper limit to the number of signal events in the null signal hypothesis for the $\tau \rightarrow \mu\gamma$ and $\tau \rightarrow e\gamma$ decays in the 3x1 topology.

No estimate is given for the $\tau \rightarrow e\gamma$ search when additional photons are allowed in the event. As already mentioned, relaxing the requirement on the presence of additional photons can be confidently done for the muon channel, but not for the electron one, as more studies are required to correct for bremsstrahlung effects.

The Feldman-Cousins method allows us to provide a simple estimate of our sensitivity, but no consideration is made for the shape of the signal and background distributions. In a full-fledged analysis, such as Belle's, more advanced techniques that take into account the shape of the signal and background distributions must be used. For example, in the Belle analysis the estimate of the number of signal and background events is performed through an unbinned maximum likelihood fit to the probability density functions (PDFs). In this case particular care should be given to the modeling of the background PDFs which must be extracted from appropriately-chosen sidebands.

Another group of the Belle II collaboration carried out a parallel analysis for the measurement of the $\tau \rightarrow \ell\gamma$ decay in the 1x1 topology. The analysis strategy adopted for the 1x1 topology is similar to the one in the Belle's result. This study predicts, for the muon channel and our target luminosity of 500 fb^{-1} , 20 background events in the signal region; the upper limit on the signal events, estimated with the same method as above, is $\text{UL}(N_{sign}) = 8.5$. The signal efficiency in this topology is 7.59%.

The above signal efficiencies are relative to the full τ decay and incorporate the tag branching fraction, which is $\mathcal{B}(\tau \rightarrow 3\pi(\pi^0)\nu) \simeq 14.56\%$ for a 3-prong tag and $\mathcal{B}(\tau \rightarrow e\nu_\tau\nu_e) + \mathcal{B}(\tau \rightarrow \pi(\pi^0)\nu) \simeq 67.85\%$ for a 1-prong (the muon channel is vetoed). Thus, the efficiencies relative to the respective tag are 16.5% and 11.2%, respectively, for a 3-prong and 1-prong tag. It can be seen that our selection is more efficient at selecting its particular tag, as expected, since the background to the 3-prong process is entirely reducible, while to one to the 1-prong is not.

5.1.2 UPPER LIMIT TO $\mathcal{B}(\tau \rightarrow \mu\gamma)$

A 90% C.L. upper limit can be set on the $\mathcal{B}(\tau \rightarrow \mu\gamma)$ branching fraction using:

$$\mathcal{B}(\tau \rightarrow \ell\gamma) = \frac{N_{sign}}{2 \cdot \mathcal{L} \cdot \sigma_{\tau\tau} \cdot \epsilon(t)} \quad (5.1)$$

By using eq (5.1), we can set the upper limit to

$$\mathcal{B}(\tau \rightarrow \mu\gamma) < 3.2 \cdot 10^{-7} \quad (5.2)$$

for the 3x1 topology and to

$$\mathcal{B}(\tau \rightarrow \mu\gamma) < 1.2 \cdot 10^{-7} \quad (5.3)$$

for the 1x1 topology.

A combination of the two channels is not trivial, but, for a rough estimate of the gain in sensitivity when including more topologies, we can assume a total signal efficiency

$$\epsilon_{tot} = \epsilon_{1prong} + \epsilon_{3prong} \quad (5.4)$$

and a total number of background events

$$N_{bkg,tot} = N_{bkg,1prong} + N_{bkg,3prong} \cdot \quad (5.5)$$

With the method above described, we can now set the new upper limit for the combination:

$$\mathcal{B}(\tau \rightarrow \mu\gamma) < 1.0 \cdot 10^{-7} \cdot \quad (5.6)$$

5.2. SYSTEMATIC UNCERTAINTIES

In this case, the addition of the 3-prong tag channel thus improves the sensitivity by 20%.

5.2 SYSTEMATIC UNCERTAINTIES

There are a number of effects that can systematically influence our measurement. Prescriptions for systematic uncertainties are provided by a dedicated group of the Belle II collaboration, the Physics Performance group. Most of the systematic effects are estimated from dedicated analyses made on control samples.

In our analysis, these uncertainties can affect the overall signal efficiency either directly or by altering the distributions for the variables of interest. The main contributions come from tracks and photon reconstruction efficiencies, photon energy calibration, luminosity and trigger efficiencies and the background PDF modeling. The estimated value of the signal efficiency in simulations is thus corrected in data for these effects, each carrying an uncertainty reported below.

The measurement of the Belle II track reconstruction efficiency uses τ -pair events, in which one τ decays as $\tau \rightarrow \ell \nu_\ell \nu_\tau$ (leptonically), while the other τ as $\tau \rightarrow 3\pi \nu_\tau + n\pi^0$ (hadronically). One pion track is selected for study, while the other three charged particles act as a tag: the reconstruction efficiency for the track can be then estimated on data. The uncertainty of 0.3% is assigned per track, for a total uncertainty of 1.2% for our analysis.

The efficiency in photon reconstruction is estimated using the radiative $e^+e^- \rightarrow \mu^+\mu^-\gamma$ process by studying reconstructed photons against the recoil of the $\mu^+\mu^-$ pair. The associated uncertainty is less than 1.0%. The same sample can be used to calibrate the photon energy, will require a dedicated study. From previous estimates, we can expect the associated uncertainties to be at the few percent level. The uncertainty associated to the integrated luminosity accounts approximately for 1%. The efficiency of our chosen trigger is estimated by using samples collected with independent triggers and comparing sidebands data and MC simulation. The trigger efficiency is estimated to be up to 4% for the electron channel and up to 1.5% for the muon channel, depending on the lepton momentum in the detector frame.

5.3 CONCLUSIONS

We have developed a selection for the 3-prong tag in the $\tau \rightarrow \ell\gamma$ analysis, which can be reconstructed with a better purity and efficiency than its 1-prong counterpart.

The addition of our channel improves the UL sensitivity of the search by approximately 20% demonstrating the potential of more inclusive tag approaches in this kind of analysis.

However, although our estimate for the upper limit of the $\mathcal{B}(\tau \rightarrow \mu\gamma)$ is of the same order of the BaBar result ($0.44 \cdot 10^{-7}$ with a similar amount of data), it still is not yet competitive with the limits from the previous generation of B-Factories. Further studies are then required to develop even more efficient event selections and background suppression.

Future work should focus on understanding the reason of this performance gap, incorporating additional discriminators in the selection and exploring the potential of machine-learning techniques.

References

- [1] M. Lubej. [Online]. Available: <https://github.com/mlubej/standard-model>.
- [2] G. Aad *et al.*, "Observation of a new particle in the search for the Standard Model Higgs boson with the ATLAS detector at the LHC," *Physics Letters B*, vol. 716, no. 1, pp. 1–29, 2012.
- [3] V. C. Rubin and W. K. Ford, "Rotation of the Andromeda nebula from a spectroscopic survey of emission regions," *The Astrophysical Journal*, vol. 159, pp. 379–403, 1970.
- [4] T. S. van Albada, J. N. Bahcall, K. Begeman, and R. Sancisi, "Distribution of dark matter in the spiral galaxy NGC 3198," *The Astrophysical Journal*, vol. 295, pp. 305–313, 1985.
- [5] A. G. Riess, "Observational evidence from supernovae for an accelerating universe and a cosmological constant," *The Astronomical Journal*, vol. 116, no. 3, p. 1009, 1998.
- [6] R. Davis, "Solar neutrinos. II. Experimental," *Phys. Rev. Lett.*, vol. 12, pp. 303–305, 11 Mar. 1964.
- [7] J. N. Bahcall, "Solar neutrinos. I. Theoretical," *Phys. Rev. Lett.*, vol. 12, pp. 300–302, 11 Mar. 1964.
- [8] Y. Fukuda *et al.*, "Evidence for oscillation of atmospheric neutrinos," *Phys. Rev. Lett.*, vol. 81, pp. 1562–1567, 1998.
- [9] Q. R. Ahmad *et al.*, "Measurement of the rate of $\nu_e + d \rightarrow p + e^-$ interactions produced by ^8B solar neutrinos at the Sudbury Neutrino Observatory," *Physical Review Letters*, vol. 87, no. 7, Jul. 2001.
- [10] Z. Maki, M. Nakagawa, and S. Sakata, "Remarks on the unified model of elementary particles," *Prog. Theor. Phys.*, vol. 28, pp. 870–880, 1962.

REFERENCES

- [11] B. Pontecorvo, "Mesonium and anti-mesonium," *Sov. Phys. JETP*, vol. 6, p. 429, 1957.
- [12] T. Araki *et al.*, "Measurement of neutrino oscillation with KamLAND: Evidence of spectral distortion," *Phys. Rev. Lett.*, vol. 94, p. 081 801, 2005.
- [13] Y. Ashie *et al.*, "A measurement of atmospheric neutrino oscillation parameters by Super-Kamiokande," *Physical Review D*, vol. 71, no. 11, Jun. 2005.
- [14] M. H. Ahn *et al.*, "Measurement of neutrino oscillation by the K2K experiment," *Physical Review D*, vol. 74, no. 7, Oct. 2006.
- [15] K. Abe *et al.*, "Indication of electron neutrino appearance from an accelerator-produced off-axis muon neutrino beam," *Physical Review Letters*, vol. 107, no. 4, Jul. 2011.
- [16] F. P. An *et al.*, "Improved measurement of electron antineutrino disappearance at Daya Bay," *Chinese Physics C*, vol. 37, no. 1, p. 011 001, Jan. 2013.
- [17] B. Kayser, "Neutrino physics," 2005. [Online]. Available: <https://arxiv.org/abs/hep-ph/0506165>.
- [18] T. P. Cheng and L. F. Li, *Gauge theory of elementary particle physics*. Oxford University Press, 1984, ISBN: 978-0-19-851961-4.
- [19] A. M. Baldini *et al.*, "Search for the lepton flavour violating decay $\mu^+ \rightarrow e^+ \gamma$ with the full dataset of the MEG experiment," *Eur. Phys. J. C*, vol. 76, no. 8, p. 434, 2016.
- [20] M. L. Perl, "The tau lepton," *Annual Review of Nuclear and Particle Science*, vol. 30, no. 1, pp. 299–335, 1980.
- [21] R. Barbieri, L. Hall, and A. Strumia, "Violations of lepton flavour and CP in supersymmetric unified theories," *Nuclear Physics B*, vol. 445, no. 2, pp. 219–251, 1995.
- [22] A. Masiero, S. K. Vempati, and O. Vives, "Susy seesaw and fcnc," *Nuclear Physics B - Proceedings Supplements*, vol. 137, pp. 156–168, 2004, ISSN: 0920-5632.
- [23] T. Fukuyama, T. Kikuchi, and N. Okada, "Lepton-flavor-violating processes and muon $g - 2$ in the minimal supersymmetric SO(10) model," *Phys. Rev. D*, vol. 68, p. 033 012, 3 Aug. 2003.

- [24] S. R. Choudhury, A. S. Cornell, A. Deandrea, N. Gaur, and A. Goyal, “Lepton flavor violation in the little Higgs model with t parity,” *Phys. Rev. D*, vol. 75, p. 055 011, 5 Mar. 2007.
- [25] T. Abe *et al.*, “Belle II technical design report,” 2010. [Online]. Available: <https://arxiv.org/abs/1011.0352>.
- [26] T. Hara, T. Kuhr, and Y. Ushiroda, “Belle II coordinate system and guideline of Belle II numbering scheme,” 2011. [Online]. Available: <https://indico.mpp.mpg.de/event/2308/material/0/1>.
- [27] M. Valentan, “The Silicon Vertex Detector for B-tagging at Belle II,” Ph.D. dissertation, Vienna, Tech. U., Atominst., 2013.
- [28] I. Adachi, T. E. Browder, P. Krian, S. Tanaka, and Y. Ushiroda, “Detectors for extreme luminosity: Belle II,” *Nucl. Instrum. Meth. A*, vol. 907, pp. 46–59, 2018.
- [29] T. Kuhr, C. Pulvermacher, M. Ritter, T. Hauth, and N. Braun, “The Belle II core software,” *Computing and Software for Big Science*, vol. 3, no. 1, Nov. 2018.
- [30] Y. Amhis *et al.*, “Averages of b-hadron, c-hadron, and τ -lepton properties as of 2018,” *The European Physical Journal C*, vol. 81, no. 3, Mar. 2021.
- [31] K. G. Hayes *et al.*, “Experimental upper limits on branching fractions for unexpected decay modes of the tau lepton,” *Phys. Rev. D*, vol. 25, p. 2869, 1982.
- [32] K. W. Edwards *et al.*, “Search for neutrinoless tau decays: $\tau \rightarrow e\gamma$ and $\tau \rightarrow \mu\gamma$,” *Phys. Rev. D*, vol. 55, pp. 3919–3923, 1997.
- [33] S. Ahmed *et al.*, “Update of the search for the neutrinoless decay $\tau \rightarrow \mu\gamma$,” *Phys. Rev. D*, vol. 61, p. 071 101, 2000.
- [34] B. Aubert *et al.*, “Searches for lepton flavor violation in the decays $\tau^\pm \rightarrow e^\pm\gamma$ and $\tau^\pm \rightarrow \mu^\pm\gamma$,” *Phys. Rev. Lett.*, vol. 104, p. 021 802, 2010.
- [35] A. Abdesselam *et al.*, “Search for lepton-flavor-violating tau-lepton decays to $\ell\gamma$ at Belle,” *JHEP*, vol. 10, p. 19, 2021.
- [36] R. Aaij *et al.*, “Search for the lepton flavour violating decay $\tau^\pm \rightarrow \mu^\pm\mu^+\mu^-$,” *JHEP*, vol. 02, p. 121, 2015.
- [37] B. Aubert *et al.*, “Measurements of the tau mass and the mass difference of the τ^+ and τ^- at BABAR,” *Phys. Rev. D*, vol. 80, p. 092 005, 2009.

REFERENCES

- [38] K. Hayasaka *et al.*, “New search for $\tau \rightarrow \mu \gamma$ and $\tau \rightarrow e \gamma$ decays at Belle,” *Phys. Lett. B*, vol. 666, pp. 16–22, 2008.
- [39] H. Albrecht *et al.*, “A measurement of the tau mass,” *Phys. Lett. B*, vol. 292, pp. 221–228, 1992.
- [40] A. J. Bevan *et al.*, “The physics of the B factories,” *Eur. Phys. J. C*, vol. 74, p. 3026, 2014.
- [41] S. Jadach, B. F. L. Ward, and Z. Was, “The precision Monte Carlo event generator KK for two-fermion final states in $e^+ e^-$ collisions,” *Comput. Phys. Commun.*, vol. 130, pp. 260–325, 2000.
- [42] ———, “Coherent exclusive exponentiation for precision Monte Carlo calculations,” *Phys. Rev. D*, vol. 63, p. 113 009, 2001.
- [43] G. Balossini, C. M. Carloni Calame, G. Montagna, O. Nicrosini, and F. Piccinini, “Matching perturbative and parton shower corrections to Bhabha process at flavour factories,” *Nucl. Phys. B*, vol. 758, pp. 227–253, 2006.
- [44] G. Balossini, C. Bignamini, C. M. C. Calame, G. Montagna, O. Nicrosini, and F. Piccinini, “Photon pair production at flavour factories with per mille accuracy,” *Phys. Lett. B*, vol. 663, pp. 209–213, 2008.
- [45] C. M. Carloni Calame, C. Lunardini, G. Montagna, O. Nicrosini, and F. Piccinini, “Large angle Bhabha scattering and luminosity at flavor factories,” *Nucl. Phys. B*, vol. 584, pp. 459–479, 2000.
- [46] C. M. Carloni Calame, “An improved parton shower algorithm in QED,” *Phys. Lett. B*, vol. 520, pp. 16–24, 2001.
- [47] C. M. Carloni Calame, G. Montagna, O. Nicrosini, and F. Piccinini, “Status of the BabaYaga event generator,” *EPJ Web Conf.*, vol. 218, p. 07 004, 2019.
- [48] F. A. Berends, P. H. Daverveldt, and R. Kleiss, “Radiative corrections to the process $e^+ e^- \rightarrow e^+ e^- \mu^+ \mu^-$,” *Nucl. Phys. B*, vol. 253, p. 421, 1985.
- [49] ———, “Complete lowest order calculations for four-lepton final states in electron-positron collisions,” *Nucl. Phys. B*, vol. 253, pp. 441–463, 1985.
- [50] ———, “Monte Carlo simulation of two-photon processes. 2. Complete lowest order calculations for four-lepton production processes in electron-positron collisions,” *Comput. Phys. Commun.*, vol. 40, pp. 285–307, 1986.

- [51] S. Uehara, “TREPS: A Monte-Carlo event generator for two-photon processes at e^+e^- colliders using an equivalent photon approximation,” Jul. 1996. arXiv: 1310.0157 [hep-ph].
- [52] M. Chrzaszcz, T. Przedzinski, Z. Was, and J. Zaremba, “TAUOLA of τ lepton decays framework for hadronic currents, matrix elements and anomalous decays,” *Comput. Phys. Commun.*, vol. 232, pp. 220–236, 2018.
- [53] E. Barberio and Z. Was, “PHOTOS: A universal Monte Carlo for QED radiative corrections. Version 2.0,” *Comput. Phys. Commun.*, vol. 79, pp. 291–308, 1994.
- [54] S. Agostinelli *et al.*, “GEANT4—a simulation toolkit,” *Nucl. Instrum. Meth. A*, vol. 506, pp. 250–303, 2003.
- [55] G. Punzi, “Sensitivity of searches for new signals and its optimization,” *eConf*, vol. C030908, MODT002, 2003.
- [56] M. J. Kochenderfer and T. A. Wheeler, *Algorithms for Optimization*. The MIT Press, 2019, pp. 129–130, ISBN: 9780262039420.
- [57] G. J. Feldman and R. D. Cousins, “Unified approach to the classical statistical analysis of small signals,” *Physical Review D*, vol. 57, no. 7, pp. 3873–3889, 1998.

Acknowledgments

I would like to thank to my supervisors, Prof. F. Forti and Dott. F. Tenchini, who guided me during these months of thesis. I am particularly grateful to Prof. Forti for his precious teachings and suggestions, and to Dott. Tenchini for having helped me, carefully and kindly, in each step of this work. I would also like to thank the entire Belle II group of Pisa for these months of working together.